The actin-spectrin submembrane scaffold restricts endocytosis along proximal axons

Florian Wernert, Satish Babu Moparthi, Florence Pelletier, Jeanne Lainé, Eline Simons, Gilles Moulay, Fanny Rueda, Nicolas Jullien, Sofia Benkhelifa-Ziyyat, Marie-Jeanne Papandréou, et al.

To cite this version:

Florian Wernert, Satish Babu Moparthi, Florence Pelletier, Jeanne Lainé, Eline Simons, et al.. The actin-spectrin submembrane scaffold restricts endocytosis along proximal axons. Science, 2024, 385 (6711), pp.eado2032. 10.1126/science.ado2032 . hal-04678794

HAL Id: hal-04678794

https://hal.science/hal-04678794v1

Submitted on 28 Aug 2024

The actin-spectrin submembrane scaffold restricts endocytosis along proximal axons

Florian Wernert[1†], Satish Babu Moparthi[2†], Florence Pelletier[1], Jeanne Lainé[3], Eline Simons[1], Gilles Moulay[2], Fanny Boroni-Rueda[1], Nicolas Jullien[1], Sofia Benkhelifa-Ziyat[2], Marie-Jeanne Papandréou[1], Christophe Leterrier[1*‡], Stéphane Vassilopoulos[2*‡]

[1] Aix Marseille Université, CNRS, INP UMR7051, NeuroCyto, 13005 Marseille, France.

[2] Sorbonne Université, INSERM, Institute of Myology, Centre of Research in Myology, UMRS 974, Paris, France.

[3] Sorbonne Université, Department of Physiology, Faculty of Medicine Pitié-Salpêtrière, Paris, France

† and ‡: these authors contributed equally

* Corresponding authors. Email: christophe.leterrier@univ-amu.fr and s.vassilopoulos@institut-myologie.org

Abstract: Clathrin-mediated endocytosis has unique features in neuronal dendrites and presynapses. How membrane proteins are internalized along the axon shaft remains unclear. Here we focused on clathrin-coated structures and endocytosis along the axon initial segment (AIS) and their relationship to the periodic actin-spectrin scaffold that lines the axonal plasma membrane. A combination of super-resolution microscopy and platinum-replica electron microscopy on cultured neurons revealed that AIS clathrin-coated pits form within "clearings", circular areas devoid of actin-spectrin mesh. Actin-spectrin scaffold disorganization increased clathrin-coated pit formation. Cargo uptake and live-cell imaging showed that AIS clathrin-coated pits are particularly stable. Neuronal plasticity-inducing stimulation triggered internalization of the clathrin-coated pits via polymerization of branched actin around them. Thus, spectrin and actin regulate clathrin-coated pit formation and scission to control endocytosis at the AIS.

Main Text:

Membrane exchange is a ubiquitous cellular process that allows cells to interact with their environment by processes such as endocytosis, phagocytosis, exocytosis, as well as exosome release and uptake. Differentiated cells such as neurons extensively rely on endocytosis to organize their complex and compartmented morphology and sustain the synaptic vesicle cycle at the core of neuronal communication (*1*). This role explains the historical focus on presynapses as the main site of endocytosis in neurons, with a wealth of studies dissecting its molecular mechanisms and coupling to the converse process of exocytosis (*2*, *3*). Neuronal endocytosis has also been extensively studied in dendrites, where it drives receptor internalization near postsynapses (*4*, *5*) and is the source of a complex endocytic traffic (*6*).

Endocytosis in neurons is mainly achieved through clathrin-mediated endocytosis (*7*). Clathrin forms triskelia made of trimerized heavy chains and light chains that assemble via adaptor proteins to form a cage-like coat around a membrane invagination called clathrin-coated pit (CCP), before the scission of the CCP neck releases a clathrin-coated vesicle. In neurons, CCPs are found at the plasma membrane of the cell body and dendrites as well as in the vicinity of the active zone in presynapses, strengthening the prevalent view that endocytosis mainly occurs in these compartments. By contrast, little is known about the nanoscale organization or even the existence of clathrin-mediated endocytosis along the axon shaft and at the axon initial segment (AIS), the specialized compartment that constitutes the proximal part of the axon next to the neuronal cell body (*8*, *9*). It was commonly assumed that little to no endocytosis could take place along the axon shaft (*10*), a view reinforced by the presence of a dense submembrane assembly of spectrins, ankyrin G and anchored membrane proteins at the AIS, and the discovery of a dense, periodic scaffold of actin rings connected by spectrin tetramers lining the axonal plasma membrane (*11–13*).

We previously used super-resolution microscopy combined with platinum-replica electron microscopy (PREM) on unroofed neurons to reveal the ultrastructure of the periodic actin-spectrin scaffold and AIS submembrane components (*14*). Despite the presence of this dense undercoat, PREM views showed numerous CCPs present along the AIS of mature neurons, which was surprising because studies at the time only detected endocytosis in the nascent AIS in developing neurons (*15*, *16*) or under acute excitotoxic stress (*17*). More recently, robust endocytic activity at the AIS was proposed as a mechanism for membrane protein sorting, allowing the retrieval of somatodendritic proteins when they enter the axon (*18*). This prompted us to focus on the detailed architecture of CCPs at the AIS, their endocytic function, and their relationships with the actin-spectrin submembrane scaffold.

Clathrin-coated pits are present in circular clearings of the actin-spectrin scaffold at the AIS

We first visualized the distribution of CCPs with regard to the spectrin mesh at the proximal axon of neurons after 14 days in vitro, labeled for α2-spectrin and for the AIS-specific adhesion molecule neurofascin (Fig. 1A). We used Structured Illumination Microscopy (SIM), which resolves the 190-nm periodicity of the actin-spectrin scaffold as well as individual CCPs, and found that CCPs were present in areas devoid of α2-spectrin, as confirmed by the intensity profiles of averaged images centered on CCPs (Fig. 1B). The presence of CCPs in areas devoid of spectrin were also observed along the more distal axon, and similarly observed when labeling the spectrin mesh for ß2-spectrin (fig. S1, A to C). To isolate the axonal plasma membrane and associated cortical cytoskeleton without additional signal from intracellular compartments, we mechanically unroofed cultured hippocampal neurons using ultrasound (Fig. 1C). The presence of CCPs inside circular areas devoid of α2-spectrin was made clearer by the unroofing, with a distinct circular hole of α2-spectrin around CCPs seen on the average image (Fig. 1D). This exclusion pattern along the dense spectrin scaffold of axons is an extreme example of the complementary pattern between submembrane spectrins and CCPs previously observed in fibroblasts (*19*) and at the lateral membrane of epithelial cells (*20*).

We then produced platinum replicas of unroofed hippocampal neurons to visualize the ultrastructure of CCPs at the AIS by PREM. To identify the axonal process stemming from unroofed cell bodies, we located the characteristic fascicles of AIS microtubules (Fig. 1E). High-magnification PREM views of the axonal membrane-associated cytoskeleton revealed the presence of characteristic actin rings embedded in a dense spectrin mesh as previously described (*14*), but also provided views of CCPs at the AIS, with their characteristic honeycomb pattern (Fig. 1E). In agreement with super-resolution fluorescence microscopy, CCPs formed on a patch of bare plasma membrane, forming a circular "clearing" of the actin-spectrin scaffold. These clearings were devoid of proteinaceous material as if the mesh had been pushed out, save one or two actin filaments that were often seen reaching the central CCP (Fig. 1F). All AIS CCPs were found at the center of spectrin clearings that measured 330 ± 7.0 nm in diameter, while the CCPs measured 83 ± 1.5 nm (Fig. 1G; all further exact mean ± SEM values together with statistics can be found in the Data S1 supplemental file). Consistent with a role of cortical actin in clathrin-mediated endocytosis (*21*), sparse filaments were found to interact with CCPs in all neuronal compartments. However, we only observed the circular clearings of the actin-spectrin scaffold in axons -- they were absent from cell body and dendrites that lack such a dense undercoat (fig. S1C).

Molecular architecture of CCPs and actin-spectrin clearings at the AIS

We next focused on the detailed architecture of the circular clearings in the actin-spectrin mesh. Along the AIS, we could find examples of empty clearings, as well as clearings presenting nascent CCPs at various budding stages: empty clearing or containing nascent, mature single, or multiple CCPs (Fig. 2A). Clearings containing single mature pits were the major population, and no change in clearing diameter was measured between maturation stages (Fig. 2B). This suggests that CCPs form in existing clearings rather than induce their formation. We detailed the components and organization of the AIS CCPs and actin-spectrin clearings using Single Molecule Localization Microscopy (SMLM), alone and in correlation with PREM. 3D Stochastic Optical Reconstruction Microscopy (STORM) of clathrin in intact neurons revealed the presence of CCPs distributed around the circumference of the AIS (fig. S2, A to C), although the grazing illumination used in SMLM resolves the CCPs along the ventral plasma membrane more clearly -- the only CCPs remaining after unroofing (fig. S2, D to F). Point-Accumulation in Nanoscale Topography (PAINT) allowed us to image CCPs and α2-spectrin simultaneously in 3D at ~20 nm resolution (Fig. 2, C to E). This confirmed the presence of CCPs in areas devoid of the spectrin mesh, both on in-plane views and transverse sections of the AIS (Fig. 2E). In addition, we used 3D-PAINT to show that the adaptor protein complex AP2 colocalizes to CCPs along the AIS (fig. S2, G to I), as classically described (*22*, *23*).

To further dissect the organization of the submembrane scaffold components around CCP-containing clearings, we performed correlative STORM-PREM. After unroofing and fixation of neurons, we labeled and imaged a given AIS component by STORM, then produced platinum replicas of the same unroofed neurons and observed them by PREM (*14*). We validated our correlative approach by using an anti-clathrin antibody to label CCPs at the AIS. The resulting overlays show how we can precisely correlate the 100-nm CCPs on both STORM and PREM images, although the anti-clathrin immunolabeling obscures the characteristic honeycomb pattern of the CCPs (fig. S2J). We then stained the AIS-specific ß4-spectrin, localizing fluorescence clusters corresponding to the center of the spectrin tetramers within the dense mesh that surrounds CCP-containing clearings (Fig. 2F). We confirmed this localization using immunogold staining of ß4-spectrin, which similarly showed gold beads localized within the dense mesh (Fig. 2G). Turning to correlative STORM-PREM of actin, we observed fluorescent phalloidin delineating the 190 nm-spaced actin rings throughout the mesh, and also actin filaments along the circular border of the mesh for some clearings, as well as individual filaments contacting the CCPs (Fig. 2, H and I). Indirect immunogold staining of actin filaments confirmed the presence of actin along the border of the clearings (fig. S2K). We also examined the nanoscale distribution of the AIS master organizer ankyrin G (ankG) that interacts with the center of the spectrin tetramers (*8*). Correlative STORM-PREM and immunogold labeling showed that ankG is present within the spectrin mesh, including around the CCP-containing clearings (fig. S2, L and M). Thus, in addition to forming a periodic actin-spectrin lattice, the AIS membrane-associated scaffold accommodates the presence of CCPs on the plasma membrane by forming circular clearings, with spectrins pushed away from the clearings and actin filaments enriched at their border (fig. S7).

The submembrane actin-spectrin mesh restricts CCP formation at the AIS

Given the formation of CCPs at the center of the circular clearings, we sought to find out if the periodic actin-spectrin mesh could control the formation of CCPs at the AIS. To test this hypothesis, we knocked down α2- and/or ß4-spectrin in neuronal cultures using short hairpin RNA (shRNA) adeno-associated viruses (AAVs). These AAVs could knock down spectrins efficiently, as shown by immuno blots (fig. S3A) and immunolabeling (fig. S4, A to D). In addition, AAV-expressed shRNAs against α2-spectrin, ß4-spectrin or a combination of both disorganized the periodic scaffold, as shown by the loss of periodicity for actin rings along the AIS and proximal axon (fig. S4, E to J). PREM views of unroofed neurons depleted for α2-

and/or ß4-spectrin showed a lack of submembrane spectrin mesh, with only actin filaments visible and the presence of numerous CCPs (Fig. 3A). Quantification confirmed that depletion of spectrins increased the density of CCPs two to three times in comparison with controls (Fig. 3C; please refer to the Data S1 supplemental file for exact values), while measurement of membrane occupation in three categories (organized mesh, disorganized mesh, bare membrane) revealed increased areas of disorganized mesh and bare membrane area (Fig. 3D). Thus, the dense spectrin mesh indeed restricts the formation of CCPs at the AIS plasma membrane.

We next used drugs to target CCPs, actin filaments, or the spectrin mesh and assessed their effect on CCP density. We first evaluated the density of CCPs at the AIS of treated neurons using SIM of intact and unroofed neurons labeled for clathrin and α2-spectrin (Fig. 3, D to G). Pitstop 2 is a drug that inhibits receptor-mediated endocytosis by blocking the budding of CCPs from the plasma membrane (*24*) Pitstop 2 treatment resulted in an increase of the CCP density at the AIS compared to controls, both in intact and unroofed neurons. Treatment with swinholide A, which inhibits new actin filament assembly and disassembles existing ones (*14*, *25*), did not result in a significant increase in CCP density. Diamide is a drug that causes oxidation of spectrins and disruption of their submembrane arrangement (*26*) Acute diamide treatment resulted in a significant increase in CCP density in both intact and unroofed neurons, similar to the effect of Pitstop 2 (Fig. 3, D to G).

PREM views of unroofed neurons allowed to characterize the effect of drugs at the ultrastructural level (Fig. 3H): more clearings containing multiple CCPs were observed after Pitstop 2 treatment, swinholide A treatment caused the disappearance of actin rings and maintenance of the spectrin mesh after, and diamide treatment caused precipitation of spectrins into reticulated aggregates , leaving numerous patches of bare accessible membrane. Quantification from PREM views confirmed the SIM data for the effect of drugs on CCP density

(Fig. 3I), while measurement of membrane occupation revealed the subtle effect of swinholide contrasting with the larger effect of diamide on spectrin organization (Fig. 3J). Overall, perturbation experiments showed that CCP formation at the AIS is not substantially affected by actin disassembly, likely because it leaves the AIS spectrin organization relatively intact (*14*). By contrast, disorganization of the spectrin mesh increases the density of CCPs at the AIS, suggesting that the disorganization of the spectrin scaffold and its defined clearings makes the plasma membrane more accessible, resulting in the assembly of more CCPs.

To assess if the regulation of CCPs formation by the dense actin/spectrin mesh along the proximal axon is specific to neurons, we performed similar perturbation experiments in Rat2 fibroblasts. In these cells, most of the plasma membrane is readily accessible, with the presence of loose disordered α2- and ß2-spectrin networks as well as areas exhibiting denser spectrin arrays (*19*, *27*). PREM views of unroofed fibroblasts showed abundant clathrin-coated structures (CCSs) over their inner surface, with more diverse clathrin structures than in neurons (fig. S5A), ranging from flat to fully curved endocytic pits (*28*, *29*). Using immunogold labeling of α2- and ß2-spectrin as well as correlative fluorescence microscopy and PREM, we found that spectrins localized on the cortical mesh in the vicinity of CCSs, directly associating with actin filaments into polygonal networks (fig. S5, B and C). Short interfering RNAs (siRNAs) could efficiently deplete α2- and ß2-spectrin without affecting clathrin heavy chain expression levels (fig. S3, B to D) and resulted in a significant increase in the density of CCSs at the ventral plasma membrane, as visualized by PREM after unroofing (fig. S5, D and F). Disorganization of submembrane spectrins with diamide also increased the density of CCSs in fibroblasts (fig. S5, E and G), confirming that the loose spectrin mesh negatively regulates the formation of CCSs. Actin filaments disruption with swinholide A had the largest effect on CCS density (fig. S5F) and was able to completely disorganize the submembrane mesh compared to the partial disorganization induced by α2-spectrin knockdown (fig. S5G). This suggests that in the absence of the dense spectrin mesh found along the axon of neurons, inhibition of endocytosis by actin disassembly can induce a striking accumulation of endocytic structures all over the bare plasma membrane of these non-neuronal cells.

Endocytic cargo concentrates in stalled CCPs at the surface of the AIS

Owing to possible variations in scission efficiency, CCP density at the plasma membrane does not directly translate into amount of endocytosis occurring in a cell: for example, Pitstop 2 treatment leads to more stalled CCPs at the membrane and completely inhibits endocytosis by blocking CCP scission (*24*). Thus, we sought to probe the extent of clathrin-mediated endocytosis directly after perturbation of the actin-spectrin submembrane scaffold. We first assessed this in Rat2 fibroblasts using a classic fluorescent transferrin uptake experiment. Knockdown of α2- and/or ß2-spectrin did not perturb the expression level of transferrin receptors (fig S3E), and significantly increased the uptake of transferrin (fig. S5, I and J). By contrast, treatment of fibroblasts with Pitstop 2 and swinholide A, which increased the density of CCPs (see above), efficiently inhibited the endocytosis of fluorescent transferrin (fig. S5K).

We then aimed to assess endocytosis at the AIS of neurons by visualizing the uptake of fluorescent cargo. Incubation of neuronal cultures with fluorescent transferrin for up to 1h resulted in its accumulation within the cell body and dendrites, but no endocytosed transferrin could be detected along the proximal axon (Fig. 4A), consistent with the reported absence of transferrin receptors from the axon (*10*, *30*, *31*). To detect endocytic processes independently of any specific receptor, we thus used fluorescent 10 kDa dextran as a fluid phase marker (*32*): after 5 to 30 min of incubation, fluorescent dextran clusters were readily detected along the dendrites and the proximal axon (Fig. 4B). Close inspection of SIM images revealed that a fraction of these dextran clusters along the proximal axon of intact neurons were colocalized with CCPs, an observation confirmed by averaged images centered on CCPs, which showed the selective enrichment in dextran at CCPs (Fig. 4C). To verify that a significant proportion of dextran clusters were not found in endosomes, but trapped at the cell surface in CCPs, we unroofed neurons after dextran feeding and before fixation to remove the intracellular compartments. SIM images showed that most of the dextran clusters now colocalized with CCPs after unroofing (Fig. 4D). We confirmed that a major population of dextran clusters were still present at CCPs after 30 min of feeding by obtaining correlative SIM-PREM images of unroofed neurons, which showed colocalization of fluorescent dextran clusters at CCPs on PREM views (fig. 4E). Thus, the numerous CCPs found in spectrin mesh clearings along the AIS are stalled at the plasma membrane and not efficiently engaged in endocytosis.

We then wanted to test if perturbation of the actin-spectrin mesh, which increases the density of CCPs by increasing membrane accessibility (see Fig. 3), induces more endocytosis or just more stalled CCPs at the AIS surface. We treated neurons with Pitstop 2, swinholide A, or diamide, combining treatments with a dextran uptake assay. Neurons were kept intact before fixation, labeling, and imaging by SIM (Fig. 4, F and G) or unroofed before fixation (Fig. 4, H and I). In intact neurons, inhibition of CCP scission with Pitstop 2 resulted in a decreased density of dextran clusters, while actin disassembly by swinholide A did not significantly change this density (Fig. 4G). In unroofed neurons that reveal the surface dextran within stalled CCPs, both Pitstop 2 and swinholide A did not affect dextran cluster density, suggesting that the decrease in intact neurons for Pitstop 2 was because of inhibited endocytosis (Fig. 4I). Diamide treatment resulted in an increased density of dextran clusters both in intact and unroofed neurons, suggesting that the enhanced formation of CCPs after disorganization of the spectrin mesh is not followed by a substantial increase in endocytosis (Fig. 4, G and I). Disorganization of the actin-spectrin mesh thus allows for the formation of more CCPs at the AIS membrane, but these CCPs appear to remain as stalled structures not actively engaged in endocytosis.

Live-cell super-resolution microscopy reveals static CCPs along the AIS and proximal axon

If CCPs are present at the AIS but rarely result in scission and conclusive endocytosis, they should be long-lived and seen as stable structures by live-cell imaging. To visualize the dynamics of CCPs together with the periodic actin-spectrin scaffold along the proximal axon, we used live-cell TIRF-SIM (*33*) of neurons transfected with clathrin light chain (CLC)-mCherry and EGFP-ß2-spectrin (Fig. 5A; Movie S1). The ~110 nm lateral resolution of TIRF-SIM could clearly resolve individual CCPs and the 190-nm periodicity of ß2-spectrin along the AIS and proximal axon, and low intensity illumination coupled to deep learning-based denoising allowed to image every 20s for 20 minutes. The resulting movies (Movie S1), visualization of the dynamics via kymographs (static CCPs appear as vertical lines, Fig. 5B) or time-color coded projections (static CCPs appear as white dots, Fig. 5C) demonstrate how CCPs are more stable at the AIS compared to the dendrites and cell body of the same neuron, with most AIS CCPs being present during the full 20 minutes of imaging. Temporal autocorrelation analysis of CLC-mCherry intensity profiles from several movies confirmed this visual impression, with a higher temporal stability of CLC-mCherry at the AIS compared to the cell body and dendrites (Fig. 5D).

To confirm this specific stability of AIS CCPs and avoid potential stabilizing effects of overexpressed clathrin or spectrin, we next used a modified AAV-mediated HiUGE strategy (*34*, *35*) to endogenously tag clathrin light chain with EGFP or mStayGold (*36*) in cultured hippocampal neurons, and imaged clathrin dynamics using super-resolution spinning disk microscopy (Fig. 5E; Movie S2). The enhanced temporal resolution (one frame every 5s for 10 min) allowed us to discern scission events for both static pits at the AIS (appearing as interruptions in the vertical traces on kymographs) and transient pits in dendrites (appearing as J-shaped traces in kymographs; Fig. 5F). Kymographs and time color-coded projections (Fig. 5G) showed that endogenously-tagged CCPs are more stable at the AIS compared to the dendrites and cell body, an observation confirmed by temporal autocorrelation analysis of clathrin dynamics from several neurons (Fig. 5H). Thus, CCPs are specifically stabilized at the AIS of neurons, consistent with the restrained endocytic activity observed using cargo uptake.

Endocytosis at the AIS can be triggered by plasticity-inducing stimulation

So far, we have demonstrated that the actin-spectrin scaffold regulates the formation of CCPs at the AIS, but that these CCPs are long-lived, stalled structures. We reasoned that this could allow AIS endocytosis to be “ready-to-go” but dependent on a physiological trigger. It was recently shown that a brief application of NMDA induces increased neuronal activity and long-term depression (LTD), in turn causing structural AIS plasticity driven by $\mathrm{Na_V}1.2$ voltage-gated sodium channel endocytosis along the distal AIS (*37*). We thus wanted to test if this upregulated AIS endocytosis results from a rearrangement of the actin-spectrin mesh and engagement of CCPs into conclusive endocytosis. Neurons were stimulated with NMDA (50 µM, 4 min) before a resting and dextran uptake steps (fig. S6A). Quantification of CCP and dextran cluster densities from SIM images of intact and unroofed neurons (Fig. 6, A to D) showed that NMDA stimulation modestly increased the density of CCPs at the AIS compared to controls. By contrast, NMDA stimulation induced a significant increase in dextran cluster density in intact neurons (Fig. 6C), whereas it did not change the detected density of surface dextran clusters (Fig. 6D). This indicated that the extra dextran clusters in the intact condition are endocytosed, and suggests that NMDA stimulation can trigger endocytosis from existing CCPs at the AIS membrane. We confirmed by performing an uptake experiment using MemGlow/MemBright, a fluorescent probe to stain the plasma membrane and endocytic compartments during the uptake assay (*38*, *39*). After NMDA stimulation and rest, numerous small, round endosomes were detected within the AIS, compared to the fainter tubule-vesicular profiles seen in control neurons (Fig. 6E).

We next visualized the submembrane ultrastructure of NMDA-treated neurons with PREM. High-magnification images of unroofed proximal axons revealed a partial disorganization of the spectrin mesh compared to control, and the presence of CCPs with normal morphology (Fig. 6F). We observed branched actin filaments surrounding CCPs (see fig. S6B for another example), which we quantified by measuring the area of clearings occupied by branched actin (Fig. 6G). Co-application of latrunculin A (LatA, fig.S6A) during the whole experiment abolished the formation of these branched actin nests around CCPs by inhibiting the polymerization of new actin filaments (Fig. 6, F and G). We used SIM of unroofed neurons to confirm the appearance of clusters of actin around clathrin-coated pits in holes of the ß4-spectrin labeling after NMDA stimulation, clusters that are eliminated by LatA (Fig. 6H). In addition to the formation of actin nests, close examination of PREM views of NMDA-treated neurons showed that the moderate increase in CCP density (Fig. 6I), which is consistent with the effect seen on SIM images (see Fig. 6C), corresponded to an elevation of the average number of CCPs per clearing (Fig. 6J) and a significantly increased diameter of the clearings (fig. S6C). This could be because of increased dynamics of CCP formation and scission from existing clearings thereby resulting in the observed elevated endocytosis. Quantification of the membrane organization showed no significant change after NMDA treatment, with most of the membrane consisting of organized mesh, while co-application of LatA induced a slight increase of bare membrane areas (fig. S6D). To refine this assessment, we used STORM to image NMDA-treated, intact neurons stained for ß4-spectrin (fig. S6, E and F). This revealed that the periodicity of the spectrin mesh was attenuated, but still detected after NMDA treatment (fig. S6, G and H).

Thus, NMDA treatment leads to polymerization of branched actin nests around CCPs in clearings, which is correlated with an increase in endocytosis along the AIS. To demonstrate that these actin nests are driving the engagement of CCPs toward conclusive endocytosis, we used co-application of LatA during NMDA stimulation and rest followed by dextran feeding (Fig. S6A). LatA slightly reduced the density of CCPs below that of the control as measured by SIM on intact neurons (Fig. 6L), but the density of CCPs measured on PREM images remained constant (Fig. 6I), indicating that actin polymerization could also act at the level of CCP formation, but primarily acts on CCP fission. In addition, LatA was able to reverse the effect of NMDA on dextran cluster densities, bringing their values down to control values (Fig. 6, K and M). Thus, the newly polymerized actin plays a role in the triggering of endocytosis by the plasticity-inducing NMDA treatment.

Discussion

The AIS and proximal axon are neuronal compartments where endocytosis has long been overlooked. We discovered that in the AIS, CCPs form on bare areas of the plasma membrane that are precisely delimited by a circular clearing of the actin-spectrin undercoat. These ~300 nm clearings are scattered across the inner surface of the AIS and proximal axon, inserted within the previously described periodic scaffold of actin rings connected by spectrin tetramers (*14*). They exhibit a specific organization: actin filaments are present at the border of the clearings, crosslinked by spectrins and ankyrin that form an outer polygonal arrangement. In addition, a single actin filament is often seen to enter the clearing and contact the central CCP (Fig. S7). We propose that clearings are structures that allow the formation of CCPs by providing access to the AIS plasma membrane. The formation of CCPs in membrane areas devoid of spectrins was previously shown by diffraction-limited fluorescent microscopy in spectrin-dense regions of fibroblasts (*19*), and along the lateral membrane of epithelial cells (*20*) – it makes all the more sense along axons where the spectrin mesh is particularly dense.

What is the respective role of the submembrane actin and spectrin in defining the patterns of CCP formation? An inhibitory role of spectrins on CCP formation and subsequent endocytosis has been proposed for fibroblasts (*19*) and endocytosis is negatively controlled by the ankyrin/spectrin domains at the lateral membrane of epithelial cells (*20*). Here, we demonstrate that spectrin knockdown or disorganization by diamide directly upregulates CCP formation in fibroblasts and along the AIS in neurons, establishing the spectrin mesh as an insulating layer restricting CCP formation. Indeed, the existence of clearings containing various stages of nascent CCPs and the increase in CCP density after spectrins knockdown or disruption suggests that the spectrin mesh regulates the formation of CCPs by defining the location and density of these clearings. Actin on the other hand has been shown to be important for the late stages of clathrin-mediated endocytosis (*21*, *40*), as confirmed by the presence of numerous stalled CCPs in fibroblasts after swinholide A treatment. In our experiments, swinholide A is not able to alter the density of CCPs significantly along the AIS, suggesting that the remaining spectrin mesh is the primary factor for the formation of clearings and CCPs. Beyond the AIS, the periodic actin-spectrin scaffold is likely to regulate endocytosis along the whole axon, as shown by the enhanced endocytosis of cannabinoid receptors after activation in neurons depleted for ß2-spectrin, a part of the distal axon periodic scaffold (*41*).

In addition to the insulating effect of the spectrin mesh on CCP formation, our results suggest that a second level of regulation is present to control endocytosis at the AIS. We found that CCPs that do form in mesh clearings along the AIS are unusually long-lived and do not readily engage in conclusive endocytosis, accumulating cargoes at the AIS surface. A signal is necessary to unlock these CCPs and engage them in conclusive endocytosis: we found that a chemical long-term depression protocol based on NMDA stimulation, previously shown to induce endocytosis at the distal AIS (*37*), can indeed provide this signal and trigger the scission of stalled CCPs (Fig. S7). In this second level of regulation, actin seems to play a prominent role, as shown by the formation of dense branched actin nests around CCPs in clearings that are necessary for increased endocytosis. This role for branched actin in CCP maturation and scission is consistent with the "edge pushing" model recently proposed for cortical actin around CCPs (*21*), and we speculate that the isolated actin filaments we consistently saw contacting CCPs inside clearings in resting neurons might be the nucleating structure for these actin nests. It will be important for future studies to decipher the upstream pathway that connect synaptic NMDA activation to local actin polymerization at the AIS clearings.

What could be the functional relevance of these two levels of regulation of endocytosis at the AIS by the submembrane scaffold? Firstly, it implies that the steady-state amount of endocytosis at the AIS is low in mature neurons. This is consistent with the stability of AIS membrane proteins (*42*) and the existence of mechanisms inhibiting their endocytosis (*15*); it suggests that the recently proposed role of AIS endocytic retrieval and degradation in the polarized sorting of somatodendritic proteins might primarily occur in developing neurons (*18*). Secondly, the presence of pre-positioned, static endocytic spots within the dense architecture of the AIS can facilitate the regulation of AIS membrane proteins (sodium channels, neurofascin) that are bound to the remarkably stable ankyrin/spectrin scaffold (*43*). Endocytosis of these proteins would require two simple steps that don't imply profound structural rearrangements: phosphorylation-dependent detachment from ankyrin G (*44*, *45*) allowing them to diffuse into the nearest CCPs, followed by triggered engagement of stalled CCPs into conclusive endocytosis. This “ready to go” mechanism is an attractive hypothesis to explain how the AIS length or position can be modified over a short time after physiological stimuli (*46*). Overall, our results support a model where CCPs form along the AIS in clearings of the actin-spectrin scaffold, where they are stabilized as long-lived structures with low endocytic activity at steady-state. Efficient endocytosis can be triggered by physiological signals, allowing rearrangement of the AIS membrane content or internalization of extracellular components (Fig. S7). We look forward to exploring further the mechanisms and roles of this regulated process, which is likely to have important physiological and pathological implications for neuronal organization and function.

Materials and Methods

Animals and neuronal cultures

The use of Wistar rats followed the guidelines established by the European Animal Care and Use Committee (86/609/CEE) and was approved by the local ethics committee (agreement D13-055-8). Rat hippocampal neurons were cultured following the Banker method, above a feeder glia layer (*47*). Rapidly, 12 or 18 mm-diameter round #1.5H coverslips were affixed with paraffin dots as spacers, then treated with poly-L-lysine (Sigma-Aldrich #P2636). Hippocampi from E18 rat pups were dissected and homogenized by trypsin treatment followed by mechanical trituration and seeded on the coverslips at a density of 4,000-8,000 cells/cm^2 for 3h in serum-containing plating medium. Coverslips were then transferred, cells down, to petri dishes containing confluent glia cultures conditioned in B27-supplemented (Thermo Fisher Scientific #17504044) neurobasal medium (NB, Thermo Fisher Scientific #21103049), and cultured in these dishes for up to 4 weeks. For this work, neurons were fixed at 13-16 days in vitro (div), a stage where they exhibit a periodic actin/spectrin scaffold along virtually all axons (*11*).

Fibroblast cultures and siRNA-mediated knockdown of spectrins

Rat2 fibroblasts were seeded on 18-mm glass coverslips to 80 % confluency in DMEM containing 10 % FCS, and they were incubated overnight at 37°C. Prior to transfection, cells were washed in PBS. Complexes of Lipofectamine 3000 (Thermo Fisher Scientific) and siRNA (corresponding to the shRNA sequences detailed below) were then introduced to the cells following the manufacture protocol (Thermo Fisher Scientific). The cells were left to incubate for 48 hours.

The validation of siRNAs knock-down in fibroblasts was performed by immuno blot. Rat2 cultures were lysed in a buffer (50 mM Tris-HCl, pH 7.5, 0.15 M NaCl, 1 mM EDTA, 1% NP-40) supplemented with a protein inhibitor cocktail 1:100 (Sigma-Aldrich). Samples denatured by 3 min boiling in Laemmli buffer were separated by electrophoresis on 4-12% bis-acrylamide gel (Thermo Fisher Scientific), then transferred to 0.45 µm nitrocellulose membranes (Thermo Fisher Scientific) and labeled with a primary antibody then a secondary antibody coupled to horseradish peroxidase (Trueblot immunoglobulin G HRP, Rockland). Proteins in samples were detected using Immobilon Western Chemiluminescent HRP Substrate (Sigma-Aldrich) and image acquisition was performed on a G-Box (Ozyme). The following primary antibodies were used to validate siRNA knock-down in fibroblasts: anti-α2-spectrin (mouse IgG2b clone D8B7, Biolegend #803201, 1:1000), anti-β2-spectrin (BD Biosciences #612563, mouse IgG1 against residues 2101–2189 of human β2-spectrin, 1:100), anti-clathrin (rabbit polyclonal anti-CHC, Abcam #ab21679, 1:1000), anti-TfR (mouse IgG1, Invitrogen #13-6800, 1:1000); anti-GADPH (mouse IgG1, Santa Cruz #sc-47724, 1:1000) was used as a loading control.

Plasmid constructs and neuronal culture transfection

Transfections were performed using the following constructs: clathrin-GFP and clathrin-mCherry plasmids were a gift from Subhojit Roy (*48*). The EGFP-β2-spectrin plasmid was a gift from Damaris Lorenzo (*49*). The spectrin-silencing shRNA plasmids were constructed in the pRFP-C-RS backbone (Origene). These plasmids allow cloning and expression of shRNA under a U6 promoter and co-expression of the TurboRFP red fluorescent protein under the control of a CMV promoter. Insertion of the shRNA sequences was performed using the SLIC technique using overlapping single strand oligonucleotides (*50*).

The sequences for each shRNA were:

α2-spectrin:

gATCAGTTTGTGGAAGAAACTTtcaagagAAGTTTCTTCCACAAACTGAT

β2-spectrin:

gCAGAAGAGATCTCCAACTACAtcaagagTGTAGTTGGAGATCTCTTCTG

β4-spectrin:

gCACTGGATAGCCGAGAAGGtcaagagCCTTCTCGGCTATCCAGTG

Luc (negative control):

gCGCTGAGTACTTCGAAATGTCtcaagagGACATTTCGAAGTACTCAGCG

(First g in bold-lowercase: additional g for efficient U6 transcription, underscore-lowercase: shRNA loop. A shRNA directed against the luciferase coding sequence was used as negative control).

Plasmid constructs (0.25 to 0.5 μg) per 18-mm coverslip were incubated with 1 μL of Lipofectamine 3000 (Thermo Fisher Scientific #L3000001) in 50 μL NB for 20 min at room temperature for liposomes to form, before being added to 10 div cultured hippocampal neurons, coverslips flipped cells up in FB12 dishes containing preheated NB. Neurons were incubated for 30 min at 37°C with 5% CO_2. After incubation, the neurons were returned to their origin culture dishes and left incubating for 2.5 to 3 days before imaging.

AAV production and titration

AAV viral vectors were prepared by triple transfection in HEK-293 cells using polyethyleneimine transfection agent: pSMD2 AAV vector plasmid containing the shRNA sequences detailed above, pXX6 plasmid coding for the viral sequences essential for AAV production, and p0009 plasmid coding for serotype 9 capsid. Vector particles were purified on an iodixanol gradient and concentrated on Amicon Ultra-15 100K columns (Merck-Millipore). The AAV vectors were titrated as vg per milliliter by quantitative real-time PCR using ITR2 (inverted terminal repeats) specific primers at a 60°C annealing temperature (forward 5′-CTCCATCACTAGGGGTTCCTTG-3′ and reverse 5′-GTAGATAAGTAGCATGGC-3′) and the MGB Taqman probe 5′-TAGTTAATGATTAACCC-3.

AAV infection for shRNA-mediated knockdown in neuronal cultures

Spectrin-silencing shRNAs in adeno-associated virus vectors (AAV) were produced and titrated by the AAV production service of Institut de Myologie (Paris). Vectors identifiers AAV9-U6SCR (p05.1 Origen scrambled sequence GAGAGCCAGATTCAATCTGACGACTATGG), AAV9-U6beta4 / p10.1 (*42*), AAV9-U6alpha2 / p09.1 (*51*), AAV9-U6-shRNA-α2+ß4-spectrin / p11.1 (both combined) targeted respectively no protein (scrambled control), β4-spectrin, α2-spectrin, α2- and β4-spectrin. The validation of shRNAs knock-down in neurons was performed by immuno blot. Cells infected with an AAV-shRNAs were resuspended in a loading buffer with DTT, diluted to 50% in ultrapure water. The samples were then heated to 90°C for 3 min. After extensive washes, samples were resolved by 7.5% sodium dodecyl sulfate–polyacrylamide gel electrophoresis, and immunoprobed with one of anti-α2-spectrin (Biolegend #803201, mouse IgG2b clone D8B7, 1:1000), anti-β2-spectrin (BD Biosciences #612563, mouse IgG1 against residues 2101–2189 of human β2-spectrin, 1:100), anti-β4-spectrin Cter (from Matthew Rasband, Baylor College of Medicine Austin TX, rabbit against residues 2237-2236, 1:100), an anti-α tubulin (Sigma-Aldrich #T5168, mouse IgG1 clone B-5-1-2, 1:1500) was used as control. Hippocampal neurons were infected at 3 div with 1.5-3.10^{10} AAV particles for 4 coverslips in a 60-mm dish and left in the presence of the AAV until fixation. The shRNAs effect on the periodicity of the axonal actin-spectrin scaffold was evaluated by fluorescence intensity quantification and autocorrelation of intensity profiles along axonal segments (https://github.com/cleterrier/Process_Profiles).

Endogenous clathrin tagging (knock-in)

We used a rat optimized version of the HiUGE method (*34*, *52*), with an adapted Donor Recognition Sequence (DRS) GCGATCGTAATCACCCGAGT-GGG. We used the homologous sequence of the protospacer used by Gao et al. to cut the clathrin light chain A subunit gene (*Clta*) as close as possible to the stop codon (5 nucleotides before):

Mouse, Gao et al : …-GGCTCTTCAGTGCACCA-**GGG**
Rat, this study: *GGT*-GGCTCTTCAaTGCACCA-**GGG**

In italics: Additional nucleotides in 5' to have a 20-nucleotid length protospacer sequence. In bold the PAM sequence on the *Clta* gene. In lowercase the nucleotide that differs from the mouse sequence. This was used for amino-terminal insertion of a sequence coding for EGFP or mStayGold with a c4 linker (*36*).

AAVs were produced by the standard triple transfection in HEK293T in the AAV9/PHP.S serotype. Small scale AAV preparations were obtained by mild lysis of HEK cells 3 days post transfection in a citrate buffer (38.1 mM citric acid, 74.8 mM $NaHCO_3$, 75 mM NaCl, 100 mM MgCl, pH 5) and neutralized subsequently with Tris-HCl pH 9.5. AAV particles were titrated by qPCR with an improved version of the Addgene SYBR green method. In brief, we used a linearized AAV plasmid as standard instead of a supercoiled plasmid and we incorporated a proteinase K step after the DNAse treatment. We usually obtained titers between 10^{11} and 10^{12} part/mL. Hippocampal neurons were triply infected after plating at 0 div and at a density of 12,000 cells/cm^2 with 10^9 AAV particles per coverslip for each 3 different AAVs: Mecp2-Cas9 AAV, clathrin-Cter sgRNA AAV and DRSR2-EGFP-ORF1 Cter HiUGE payload and left in the presence of the AAVs for 48h.

Pharmacological treatments

Treatments were applied on neurons and fibroblasts in their original culture medium at 37°C, 5% CO_2. Dimethyl sulfoxide (DMSO) 0.1% (from pure DMSO, Sigma-Aldrich #D2650) was used as a control vehicle, Pitstop 2 30 µM (from 30 mM stock in DMSO, Abcam #120687) was applied for 15 min (45 min in neuron feeding experiments), swinholide A 100 nM (from 100 µM stock in DMSO, Sigma-Aldrich #S9810) was applied for 3h, diamide 5 mM (from 1M stock in ultrapure water, Sigma-Aldrich #D3648) was applied for 15 min (45 min in neuron feeding experiments). All stock solutions were stored at −20°C. For NMDA stimulation, 14 div neurons were first incubated 5 to 15 min in 500 µL of uncomplemented neurobasal medium (NB) in a 12 wells plate at 37°C 5% CO_2, then NMDA (from 50 mM stock in ultrapure water, Sigma-Aldrich #M3262), diluted to 100 µM in preheated NB, was added to the wells for a final concentration of 50 µM. For control experiments, NB without NMDA was used. After 4 min, neurons were gently washed 3 times with 500 µL NB, then returned to their original complemented medium and incubated for 30 min. Neurons were then either fixed and stained as described in the immunocytochemistry section or incubated with an endocytosis probe as described in the uptake assays section. LatA co-application at 5 µM (from 10 mM stock in water, Merck #5163) was performed during all steps of the NMDA stimulation experiments (pre-treatment, NMDA treatment, rest, uptake).

Unroofing and fixation of fibroblasts and neuronal cultures

Unroofing was performed by sonication as previously described (*53*). Coverslips were quickly rinsed three times in Ringer+Ca (155 mM NaCl, 3 mM KCl, 3 mM NaH_2PO_4, 4.5 mM HEPES, 10 mM glucose, 2 mM $CaCl_2$, 1 mM $MgCl_2$, pH 7.2), then immersed 10s in Ringer-Ca (155 mM NaCl, 3 mM KCl, 3 mM NaH_2PO_4, 4.5 mM HEPES, 10 mM glucose, 3 mM EGTA, 5 mM $MgCl_2$, pH 7.2) containing 0.5 mg/mL poly-L-lysine, then quickly rinsed in Ringer-Ca then unroofed by scanning the coverslip with rapid (2-5s) sonicator pulses at the lowest deliverable power in KHMgE buffer (70 mM KCl, 30 mM HEPES, 5 mM $MgCl_2$, 3 mM EGTA, pH 7.2). Unroofed cells were immediately fixed in 4% PFA in KHMgE for 10 min for epifluorescence microscopy, SIM and SMLM, for 45 min for PREM of immunogold-labeled samples, and for 15 min for PREM, correlative SIM-PREM and SMLM-PREM. After fixation and rinses, all neuronal samples for PREM were placed in individual sealed transport wells containing 5 mL of KHMgE with 2% glutaraldehyde and shipped immediately the following day. Samples for correlative light microscopy-PREM were immunolabeled and imaged immediately and kept in KHMgE with 2% sodium azide (Sigma-Aldrich #08591) at 4°C for a maximum of 1.5 days before being shipped in the same manner.

Fluorescence immunocytochemistry

Fluorescence immunocytochemistry of neuronal cultures for widefield microscopy, SIM and SMLM was performed as in published protocols (*54*). Cells were fixed using 4% PFA in PEM buffer (80 mM PIPES pH 6.8, 5 mM EGTA, 2 mM $MgCl_2$) for 10 min at room temperature

(RT). After rinses in 0.1 M phosphate buffer (PB), neurons were blocked for 2-3h at RT in immunocytochemistry buffer (ICC: 0.22% gelatin, 0.1% Triton X-100 in PB), and incubated with primary antibodies diluted in ICC overnight at 4°C. After rinses in ICC, neurons were incubated with secondary antibodies diluted in ICC for 1h at RT and rinsed. Actin staining was then performed by incubating in fluorescent phalloidin at 0.5 µM for either 1h at RT or overnight at 4°C. Stained coverslips were kept in PB + 0.02% sodium azide at 4°C until imaging by SMLM. For widefield microscopy and SIM, coverslips were mounted in ProLong Glass (Thermo Fisher Scientific #P36980).

Immunofluorescence of unroofed neurons for correlative SIM-PREM was performed using a fast protocol, beginning with 3 rinses in KHMgE buffer, then 30 min blocking in detergent-free buffer (DFB: KHMgE, 1% BSA), 30 min primary antibodies incubation at RT, 3 DFB rinses with 5 min incubation between them, 30 min secondary antibodies incubation at RT, 3 DFB rinses as before, then a KHMgE rinse, keeping the unused coverslips in KHMgE at 4°C until acquired in SIM.

Immunogold labeling of unroofed samples was performed in the same detergent-free solution: samples were blocked for 30 min, incubated for 90 min with the primary antibodies diluted to 1:20, rinsed, incubated two times 20 min with the gold-coupled secondary antibodies, then rinsed.

For immunogold labeling of actin, unroofed neurons were fixed with 2% PFA in KHMgE, then quenched for 10 min in KHMgE, 100 mM glycine, and 100 mM NH4Cl. After blocking in KHMgE, 1% BSA, they were incubated with phalloidin-Alexa Fluor 488 (0.5 µM, Thermo Fisher Scientific #A12379) for 45 min, then immunolabeled using a polyclonal rabbit anti-Alexa

Fluor 488 primary antibody (1:20, Thermo Fischer Scientific #A11094) and a gold coupled goat anti-rabbit secondary antibody as described above for immunogold labeling.

Antibodies labeling, probes, and other reagents

Rabbit polyclonal anti β4-spectrin antibody (against residues 2237–2256 of human β4-spectrin, 1:500 dilution for immunofluorescence IF, 1:20 for immunogold IG) was a gift from Matthew Rasband (Baylor College of Medicine, Austin, TX). Mouse monoclonal anti β2-spectrin (clone 42, against residues 2101–2189 of human β2-spectrin, 1:100 for IF) was from BD Biosciences (#612563). Mouse monoclonal anti α2s-spectrin (clone D8B7, 1 :100 for IF) was from Biolegend (#803201). Rabbit polyclonal anti 480-kDa ankyrin G (residues 2735–2935 of rat 480-kDa ankyrin G, 1:300 for IF, 1:100 for IG) was a gift from Vann Bennett (Duke University, Durham, NC). Chicken polyclonal anti-map2 (against residues 2-314 of human map2, 1:1000 for IF) was from Synaptic Systems (#188006). Chicken polyclonal anti pan-neurofascin (against residues 25-1031 of rat neurofascin, 1:400 for IF) was from R&D System (#AF3235). Mouse monoclonal anti-neurofascin (clone A12/18, against extracellular residues 25-110 common to rat neurofascin 155 and 186, 1:250 for live staining) was from NeuroMab (#75-172). Rabbit polyclonal anti-clathrin heavy chain (against residues 1650 to C-terminus of human clathrin heavy chain, IF 1:150) was from Abcam (#ab21679). Mouse monoclonal anti-clathrin light chain (clone X22, 1:100 for IF) was from Thermo Fisher Scientific (#MA1-065); we also used clone CON.1 (1:1000 for IF) from Sigma-Aldrich (#c1985) and guinea pig polyclonal anti-clathrin light chain (1:500 for IF) from Synaptic Systems (#113004). Mouse monoclonal anti-AP2 (clone AP6, 1:100 for IF) was from Abcam (#ab2730).

Secondary antibodies and reagents

Donkey and goat anti-rabbit, anti-mouse, and anti-chicken secondary antibodies conjugated to Alexa Fluor 488, 555, and 647 were from Life Technologies or Jackson ImmunoResearch (1:200-1:400 for IF). Goat anti-rabbit and anti-mouse secondary antibodies conjugated to DNA-PAINT handles were obtained from Massive Photonics (MASSIVE-sdAB 2-PLEX). Goat anti-rabbit and anti-mouse secondary antibodies conjugated to gold nanobeads were from Aurion (15 nm gold, #815011 and #815022, respectively, 1:20 for IG) or Jackson ImmunoResearch (18 nm gold, #111-215-144 and #115-215-146, respectively, 1:15 for IG). For light microscopy, we used Alexa Fluor 488 and Alexa Fluor 647 Plus-conjugated phalloidin from Thermo Fisher Scientific (#A12379 and #A2287, respectively) and Atto488- or Atto643-conjugated phalloidin (#AD48881 and #AD643-8, respectively) from Atto-Tec. Paraformaldehyde (PFA, #15714, stock 32% in water) was from Electron Microscopy Sciences, and glutaraldehyde (#G5882, stock 25% in water) was from Sigma-Aldrich.

Transferrin, dextran and MemGlow uptake assays

For pulse-chase uptake assay of transferrin internalization in rat fibroblasts, cells were cultured on 12-mm glass coverslips in DMEM and 10% FCS to 80% confluency. Transferrin from human serum conjugated to Alexa Fluor 488 (Thermo Fisher Scientific #T3342) was used at 20 µg/mL for 10 min at 37°C. Cells were acid-stripped (0.2 M Na_2HPO_4, 0.1 M citric acid), rinsed three times in PBS, and then fixed in 4 % paraformaldehyde (PFA) for 20 min. Glass slides were mounted with coverslips using Vectashield containing DAPI (Vector Laboratories #H-1200). Regions of interest were defined based on the cell shape. Individual cells were manually outlined and corrected total cell fluorescence = integrated density - (area of selected cell × mean fluorescence of background readings) was calculated using Fiji imaging software.

For transferrin uptake experiments in neurons, cells that were incubated for 1h in Neurobasal medium, then Alexa-Fluor-647-conjugated transferrin was used (Thermo Fisher Scientific, #T23366, stock 5 mg/mL in water) diluted to 100 µg/mL in the same medium and incubated for 1h at 37°C and 5% CO_2. After incubation, the cells were quickly rinsed 3 times with pre-heated medium and fixed with PFA 4% in PEM buffer. For dextran uptake experiments, the same procedure was used, with Alexa Fluor 555-conjugated dextran 10 kDa (Thermo Fisher Scientific #D34679) diluted to 50 µg/mL in Neurobasal medium and incubated for 30 min at 37°C and 5% CO_2 before rinses and fixation. For MemGlow (commercial name of the MemBright probes) uptake experiments, MemGlow560 (Cytoskeleton Inc #MG02-02) was diluted to 200 nM (from a 100 µM stock in DMSO) in Neurobasal medium and incubated for 30 minutes at 37°C and 5% CO_2 together with 1:250 mouse anti-neurofascin antibody directed against an extracellular epitope, before rinses and fixation.

Live-cell imaging probes and AIS staining

All live-cell experiments were performed in live-cell imaging medium (Hibernate E low fluorescence, Brainbits/Thermo Fisher Scientific #NC0285514) supplemented with 3% glucose, 2% B27, and 0.5mM L-glutamine). Live-cell AIS staining was performed using a mouse anti-neurofascin antibody targeting an extracellular epitope conjugated with CF647 (Mix-N-Stain CF647 antibody labeling kit, Sigma-Aldrich #MX647S50) following the manufacturer protocol. The conjugate was diluted to 1:50 and incubated for 10 min at 37°C and 5% CO_2 before proceeding to SIM or SoRA spinning disk microscopy.

Structured illumination microscopy

SIM of neurons was performed on an N-SIM-S microscope (Nikon Instruments). The N-SIM system uses an inverted Nikon Eclipse Ti2-E microscope with a perfect focus system 4, an integrated Nikon laser launch with 405, 488, 561, and 640 nm solid-state excitation lasers, a 100X NA 1.49 oil objective (SR HP Apo TIRF), a Mad City Labs Nanodrive piezo stage and a Hamamatsu Fusion BT CMOS camera. On fixed cells, after locating a neuron of interest using low-intensity illumination, an image was acquired in 2D-SIM/TIRF-SIM (9 images per image) or 3D-SIM (15 images per z plane) mode. Reconstruction was performed using the N-SIM module in the NIS-Elements software (AR 5.30.05), resulting in a ~120 nm lateral (all modalities) and ~250 nm axial resolution (for 3D-SIM).

For live-cell SIM, live-cell imaging medium was used, and the stage was kept at 37°C by a Tokay Hit STX heater. TIRF-SIM movies were captured at a frequency of 0.05 Hz for 15 to 20 min, alternating the 488- and 561-nm illumination to image ß2-spectrin-GFP and CLC-mCherry, respectively. Movies were processed using a deep-learning based denoising module (Enhance.ai in NIS-Elements software, Nikon) using a model trained from 20 pairs of fixed samples imaged at low (10%-20%) and high (100%) laser intensities. Neurons used for model training were transfected with CLC-mCherry and EGFP-β2-spectrin, then fixed and mounted in live-cell imaging medium. Movies were stabilized using the Image Stabilizer plugin (https://imagej.net/plugins/image-stabilizer), corrected for bleaching by histogram matching (https://imagej.net/plugins/bleach-correction) and presented using the "Noice complementary" LUTs from Kevin Terretaz (CRBM, Montpellier).

For super-resolved spinning disk microscopy of Rat2 fibroblasts, images were acquired using a Nikon Ti2 microscope, driven by Metamorph (Molecular Devices), equipped with a motorized stage and a Yokogawa CSU-W1 spinning disk head coupled with a Prime 95 sCMOS camera (Photometrics) equipped with a 100X oil-immersion objective lens. Super-resolution images were obtained using the LiveSR module (Gataca Systems). DAPI, Alexa Fluor 488, Alexa Fluor

568 and Alexa Fluor 647 were sequentially excited. Z-series from the top to the bottom of fibers were sequentially collected for each channel with a step of 0.1-0.3 µm between each plane.

Live-cell super-resolved spinning-disk imaging of endogenously-tagged clathrin-EGFP in neurons was performed on a Yokogawa CSU-W1 spinning disk microscope equipped with 405, 488, 561, and 640 nm solid-state excitation lasers, a SoRa pixel reassignment module, a Ti2-E stand (Nikon), a 60X NA 1.49 oil objective, and a Fusion BT sCMOS camera (Hamamatsu). Live-cell imaging medium was used, and the stage was kept at 37°C by a stage enclosure (Okolab). After capturing a single image of the neurofascin live-cell staining using 647-nm laser excitation, super-resolved images of clathrin-GFP were obtained using 488-nm laser excitation, with the SoRa module 4X magnification lens and a camera binning of 2x2 at a frequency of 0.2 Hz. Movies were processed using a pre-trained deep-learning based denoising module embedded in the NIS-Elements software (Denoise.ai, Nikon).

STORM and PAINT

Both STORM and DNA-PAINT acquisitions were performed on an N-STORM microscope (Nikon Instruments). The N-STORM system uses an Agilent MLC-400B laser launch with 405 nm (50 mW maximum fiber output power), 488 nm (80 mW), 561 mW (80 mW), and 647 nm (125 mW) solid-state lasers, a 100X NA 1.49 objective, and an Ixon DU-897 camera (Andor). After locating an axon using low-intensity epifluorescence illumination, followed by either a STORM or DNA-PAINT acquisition using laser illumination in HiLo (grazing angle) configuration. An astigmatic lens was added to the light path to achieve 3D imaging. For STORM, stained coverslips were mounted in a silicone chamber filled with STORM buffer (Smart Buffer Kit; Abbelight), and 30,000-60,000 images (256 × 256 pixels, 15 ms exposure time) were acquired at 100% 647-nm laser power. Reactivation of fluorophores was performed during acquisition by increasing illumination with the 405-nm laser. For DNA-PAINT, stained coverslips were mounted in a Ludin chamber filled with imaging buffer (Massive Photonics). Imaging strands conjugated to Atto565 and Atto655 (Massive Photonics) were added from a starting concentration of 0.1 nM each, then adjusted to optimize blinking density. 30,000-45,000 images (256x256, 40 ms exposure time) were acquired at 25-50% laser power for 561 nm, 60-100% laser power for 647 nm by alternating frames with 561-nm and 647-nm laser excitation.

For STORM and DNA-PAINT images, acquired stacks were processed using DECODE (*55*). Briefly, PSFs were modeled using spline fitting in SMAP (Li et al., 2018) and used to simulate sequences of blinking events using characteristics (photon number range and lifetime distribution) inferred from real acquisition data from the N-STORM microscope. A PyTorch model was trained to infer the 3D coordinates and uncertainty of the simulated blinking events and then applied to the experimental acquired sequence (*55*). The resulting localizations (fitted blinking events) were filtered based on uncertainty, and drift during acquisition was corrected in 3D using a redundant cross-correlation algorithm (*56*) implemented as an independent module of SMAP (*57*). After translation of the coordinate files, image reconstructions were performed using the ThunderSTORM ImageJ plugin (*58*) in Fiji software. Custom scripts and macros were used to translate coordinate files, as well as automate image reconstruction for whole images at 16 nm/pixel for visualization and at 8 nm/pixel for cluster analysis (https://github.com/cleterrier/ChriSTORM).

Electron microscopy of platinum replica

Adherent plasma membranes from rat hippocampal neurons and rat fibroblasts grown on glass coverslips were disrupted by sonication (*53*). Unroofed cells were fixed and processed as described previously (*14*). Cells were sequentially treated with 0.5% OsO_4, 1% tannic acid, and

1% uranyl acetate prior to graded ethanol dehydration and hexamethyldisilane substitution (Sigma-Aldrich). Dried samples were rotary-shadowed with 2 nm of platinum and 6 nm of carbon using a high vacuum sputter coater (Leica Microsystems). The resultant platinum replica was floated off the glass with hydrofluoric acid (5%), washed several times with distilled water, and picked up on 200 mesh formvar/carbon-coated EM grids. Replicas on EM grids were mounted in a eucentric side-entry goniometer stage of either a transmission electron microscope operated at 80 kV (model CM120; Philips) equipped with a Morada digital camera (Olympus), or a transmission electron microscope running at 120 kV (Jeol) equipped with a Xarosa digital camera (EMSYS GmbH). Images were adjusted for brightness and contrast in Adobe Photoshop (Adobe) and presented in inverted contrast.

Correlative SIM-PREM/SMLM-PREM microscopy

Unroofed and stained samples were imaged by SIM and an objective-style diamond scriber (Leica) was used to engrave a 1 mm circle around the imaged area. Low-magnification, 10x and 40x phase and fluorescence images were taken as a reference for relocation. After the acquisition session, samples were stored, shipped and platinum replicated as described in the PREM section. After replica generation and prior to its release, the coated surface of each coverslip was scratched with a needle to make an EM grid sized region of interest containing the engraved circle. Grids were imaged with low-magnification EM to relocate the region that was previously imaged by SIM or SMLM, and high magnification EM views were taken from the corresponding axonal region. The SIM or SMLM reconstructions were mapped and aligned by affine transformation to the corresponding high-magnification EM view using the eC-CLEM plugin in ICY software (*59*).

Data quantification and analysis

Clathrin pits and dextran clusters segmentation (SIM data)

Clathrin and dextran clusters were segmented using a custom script in Fiji (*60*). After manually delineating ROIs corresponding to the proximal axon on a stack of SIM images, fluorescence within each axon ROI was thresholded (threshold levels were determined by the Moments method for clathrin and dextran intact, Otsu method for clathrin and dextran unroofed, eventually fine-tuned manually). Thresholded areas were then segmented using the StarDist plugin in Fiji (*61*), with a baseline threshold of 0.5, eventually fine-tuned manually (other StarDist parameters were: StarDist2D Versatile model, normalize bottom 0.1 top 99.8, overlap threshold 0.33). Only the clusters inside the axon ROI or overlapping it by more than half their area were kept, and segmented aggregates of several clusters were removed. The remaining clusters were quantified for area within Fiji and the quantifications exported to a CSV file for each image. The particles CSV files were analyzed in a dedicated JupyterLab notebook, pooling the experiments per condition, and performing particle area, count, density, and pixel-occupation averages.

Average image of clathrin pits and dextran clusters

The ROI sets for clusters obtained after the segmentation of SIM images were used to generate average intensity plots of clathrin pits and dextran clusters. 15x15 pixels centered areas were extracted from each ROI and averaged over all ROIs for each channel. The radial average fluorescence profile for each channel was obtained from the averaged image using the Radial Profile Extended ImageJ plugin.

Live-cell temporal autocorrelation and kymographs

Live-cell imaging movies were corrected for drift using the Image Stabilization plugin and for bleaching by histogram matching, both in Fiji. Line ROIs were traced on the axon, dendrites, and cell body using NeuronJ (*62*) on the maximum projection of the movie frames. These line ROIs

(360-390 nm line thickness) were used to generate kymographs using the KymoResliceWide plugin (https://github.com/ekatrukha/KymoResliceWide). In addition, the intensity profile along thick line ROIs was used to calculate a temporal correlation profile with the ImageCorrelationJ plugin, comparing the image similarity between all pairs of frames distant by 1, 2, …, (n-1) frames within an n-frames movie (https://www.gcsca.net/IJ/ImageCorrelationJ.html). Temporal correlation profiles were averaged for ROIs of the same type (axon, dendrite, cell body), resulting in an average temporal correlation profile for this compartment.

Morphological quantification on PREM views

Clathrin structures and branched actin filaments within clearings were manually delineated on unroofed PM pictures using ImageJ. Each object was classified and the object area was measured. For each image, the total membrane area was also measured to calculate the clathrin structure density corresponding to the object count normalized by membrane area.

Membrane occupation on PREM views

Membrane areas were manually delineated on unroofed PREM images using ImageJ and sub-divided into either organized mesh, disorganized mesh, and bare membranes (for neurons) or mesh and bare membrane (for fibroblasts). For neurons, areas that showed a distinguishable cytoskeletal network were considered as organized mesh, areas that showed undistinguishable cytoskeletal components were considered as disorganized mesh, and areas that were devoid of any cytoskeletal network were considered as bare membrane. On each image, the total membrane area was also measured to calculate the percentages of each classified membrane area.

Statistics

Individual measurement points (n) from independent experiments (N) were pooled. Intensity profiles, graphs, and statistical analyses were generated using Prism. On bar graphs, dots (if present) are averages of each independent experiment, bars or horizontal lines represent the mean, and vertical lines are the SEM unless otherwise specified. Significances were tested using one-way, non-parametric ANOVA with Kruskal-Wallis post-hoc significance testing between selected conditions. In Figures, the results of the post-hoc significance are indicated as follows: ns or ns, non-significant; *, $p < 0.05$; **, $p < 0.01$; ***, $p < 0.001$. All means, SEM and standard deviations together with statistics (number of points n, number of independent experiments N, significance of differences) are summarized in the Data S1 supplemental file.

References and Notes

1. S. Mukherjee, R. N. Ghosh, F. R. Maxfield, Endocytosis. *Physiological Reviews* **77**, 759–803 (1997).
2. D. Azarnia Tehran, T. Maritzen, Endocytic proteins: An expanding repertoire of presynaptic functions. *Current Opinion in Neurobiology* **73**, 102519 (2022).
3. S. O. Rizzoli, Synaptic vesicle recycling: steps and principles. *The EMBO Journal* **33**, 788–822 (2014).
4. M. Rosendale, D. Jullié, D. Choquet, D. Perrais, Spatial and Temporal Regulation of Receptor Endocytosis in Neuronal Dendrites Revealed by Imaging of Single Vesicle Formation. *Cell Rep* **18**, 1840–1847 (2017).
5. L. A. Catsburg, M. Westra, A. M. van Schaik, H. D. MacGillavry, Dynamics and nanoscale organization of the postsynaptic endocytic zone at excitatory synapses. *eLife* **11**, e74387 (2022).
6. C. C. Yap, B. Winckler, Spatial regulation of endosomes in growing dendrites. *Developmental Biology* **486**, 5–14 (2022).
7. S. Camblor-Perujo, N. L. Kononenko, Brain-specific functions of the endocytic machinery. *The FEBS Journal* **289**, 2219–2246 (2022).
8. M. N. Rasband, The axon initial segment and the maintenance of neuronal polarity. *Nat Rev Neurosci* **11**, 552–562 (2010).
9. C. Leterrier, The Axon Initial Segment: An Updated Viewpoint. *J Neurosci* **38**, 2135–2145 (2018).

10. R. G. Parton, K. Simons, C. G. Dotti, Axonal and dendritic endocytic pathways in cultured neurons. *J Cell Biol* **119**, 123–137 (1992).

11. K. Xu, G. Zhong, X. Zhuang, Actin, spectrin, and associated proteins form a periodic cytoskeletal structure in axons. *Science* **339**, 452–456 (2013).

12. D. N. Lorenzo, R. J. Edwards, A. L. Slavutsky, Spectrins: molecular organizers and targets of neurological disorders. *Nat Rev Neurosci* **24**, 195–212 (2023).

13. C. Leterrier, Putting the axonal periodic scaffold in order. *Curr Opin Neurobiol* **69**, 33–40 (2021).

14. S. Vassilopoulos, S. Gibaud, A. Jimenez, G. Caillol, C. Leterrier, Ultrastructure of the axonal periodic scaffold reveals a braid-like organization of actin rings. *Nat Commun* **10**, 5803 (2019).

15. T. Torii, Y. Ogawa, C.-H. Liu, T. S.-Y. Ho, H. Hamdan, C.-C. Wang, J. A. Oses-Prieto, A. L. Burlingame, M. N. Rasband, NuMA1 promotes axon initial segment assembly through inhibition of endocytosis. *J Cell Biol* **219**, e201907048 (2020).

16. A. Fréal, D. Rai, R. P. Tas, X. Pan, E. A. Katrukha, D. van de Willige, R. Stucchi, A. Aher, C. Yang, A. F. M. Altelaar, K. Vocking, J. A. Post, M. Harterink, L. C. Kapitein, A. Akhmanova, C. C. Hoogenraad, Feedback-Driven Assembly of the Axon Initial Segment. *Neuron* **104**, 305-321.e8 (2019).

17. T. Benned-Jensen, R. K. Christensen, F. Denti, J.-F. Perrier, H. B. Rasmussen, S.-P. Olesen, Live Imaging of Kv7.2/7.3 Cell Surface Dynamics at the Axon Initial Segment: High Steady-State Stability and Calpain-Dependent Excitotoxic Downregulation Revealed. *J Neurosci* **36**, 2261–2266 (2016).

18. K. Eichel, T. Uenaka, V. Belapurkar, R. Lu, S. Cheng, J. S. Pak, C. A. Taylor, T. C. Südhof, R. Malenka, M. Wernig, E. Özkan, D. Perrais, K. Shen, Endocytosis in the axon initial segment maintains neuronal polarity. *Nature* **609**, 128–135 (2022).

19. A. Ghisleni, C. Galli, P. Monzo, F. Ascione, M.-A. Fardin, G. Scita, Q. Li, P. Maiuri, N. C. Gauthier, Complementary mesoscale dynamics of spectrin and acto-myosin shape membrane territories during mechanoresponse. *Nat Commun* **11**, 5108 (2020).

20. P. M. Jenkins, M. He, V. Bennett, Dynamic spectrin/ankyrin-G microdomains promote lateral membrane assembly by opposing endocytosis. *Sci Adv* **1**, e1500301 (2015).

21. C. Yang, P. Colosi, S. Hugelier, D. Zabezhinsky, M. Lakadamyali, T. Svitkina, Actin polymerization promotes invagination of flat clathrin-coated lattices in mammalian cells by pushing at lattice edges. *Nature Communications* **13**, 6127 (2022).

22. H. T. McMahon, E. Boucrot, Molecular mechanism and physiological functions of clathrin-mediated endocytosis. *Nat Rev Mol Cell Biol* **12**, 517–533 (2011).

23. B. M. Pearse, M. S. Robinson, Clathrin, adaptors, and sorting. *Annu Rev Cell Biol* **6**, 151–171 (1990).

24. L. von Kleist, W. Stahlschmidt, H. Bulut, K. Gromova, D. Puchkov, M. J. Robertson, K. A. MacGregor, N. Tomilin, A. Pechstein, N. Chau, M. Chircop, J. Sakoff, J. P. von Kries, W. Saenger, H.-G. Kräusslich, O. Shupliakov, P. J. Robinson, A. McCluskey, V. Haucke, Role of the Clathrin Terminal Domain in Regulating Coated Pit Dynamics Revealed by Small Molecule Inhibition. *Cell* **146**, 471–484 (2011).

25. M. R. Bubb, I. Spector, A. D. Bershadsky, E. D. Korn, Swinholide A is a microfilament disrupting marine toxin that stabilizes actin dimers and severs actin filaments. *J Biol Chem* **270**, 3463–3466 (1995).

26. X.-T. Wu, L.-W. Sun, X. Yang, D. Ding, D. Han, Y.-B. Fan, The potential role of spectrin network in the mechanotransduction of MLO-Y4 osteocytes. *Sci Rep* **7**, 40940 (2017).

27. A. Ghisleni, M. Bonilla-Quintana, M. Crestani, A. Fukuzawa, P. Rangamani, N. Gauthier, Mechanically induced topological transition of spectrin regulates its distribution in the mammalian cortex. *bioRxiv*, 2023.01.02.522381 (2023).

28. J. Heuser, Three-dimensional visualization of coated vesicle formation in fibroblasts. *J Cell Biol* **84**, 560–583 (1980).

29. G. Moulay, J. Lainé, M. Lemaître, M. Nakamori, I. Nishino, G. Caillol, K. Mamchaoui, L. Julien, F. Dingli, D. Loew, M. Bitoun, C. Leterrier, D. Furling, S. Vassilopoulos, Alternative splicing of clathrin heavy chain contributes to the switch from coated pits to plaques. *J Cell Biol* **219**, e201912061 (2020).

30. P. L. Cameron, T. C. Südhof, R. Jahn, P. De Camilli, Colocalization of synaptophysin with transferrin receptors: implications for synaptic vesicle biogenesis. *Journal of Cell Biology* **115**, 151–164 (1991).

31. G. G. Farías, L. Cuitino, X. Guo, X. Ren, M. Jarnik, R. Mattera, J. S. Bonifacino, Signal-mediated, AP-1/clathrin-dependent sorting of transmembrane receptors to the somatodendritic domain of hippocampal neurons. *Neuron* **75**, 810–823 (2012).

32. L. Li, T. Wan, M. Wan, B. Liu, R. Cheng, R. Zhang, The effect of the size of fluorescent dextran on its endocytic pathway. *Cell Biol Int* **39**, 531–539 (2015).

33. P. Kner, B. B. Chhun, E. R. Griffis, L. Winoto, M. G. L. Gustafsson, Super-resolution video microscopy of live cells by structured illumination. *Nat Methods* **6**, 339–342 (2009).

34. Y. Ogawa, B. C. Lim, S. George, J. A. Oses-Prieto, J. M. Rasband, Y. Eshed-Eisenbach, H. Hamdan, S. Nair, F. Boato, E. Peles, A. L. Burlingame, L. Van Aelst, M. N. Rasband, Antibody-directed extracellular proximity biotinylation reveals that Contactin-1 regulates axo-axonic innervation of axon initial segments. *Nat Commun* **14**, 6797 (2023).

35. D. Bingham, C. E. Jakobs, F. Wernert, F. Boroni-Rueda, N. Jullien, E.-M. Schentarra, K. Friedl, J. Da Costa Moura, D. M. van Bommel, G. Caillol, Y. Ogawa, M.-J. Papandréou, C. Leterrier, Presynapses contain distinct actin nanostructures. *Journal of Cell Biology* **222**, e202208110 (2023).

36. R. Ando, S. Shimozono, H. Ago, M. Takagi, M. Sugiyama, H. Kurokawa, M. Hirano, Y. Niino, G. Ueno, F. Ishidate, T. Fujiwara, Y. Okada, M. Yamamoto, A. Miyawaki, StayGold variants for molecular fusion and membrane-targeting applications. *Nature Methods* **21**, 648–656 (2024).

37. A. Fréal, N. Jamann, J. Ten Bos, J. Jansen, N. Petersen, T. Ligthart, C. C. Hoogenraad, M. H. P. Kole, Sodium channel endocytosis drives axon initial segment plasticity. *Sci Adv* **9**, eadf3885 (2023).

38. E. Lemerle, J. Lainé, M. Benoist, G. Moulay, A. Bigot, C. Labasse, A. Madelaine, A. Canette, P. Aubin, J.-M. Vallat, N. B. Romero, M. Bitoun, V. Mouly, I. Marty, B. Cadot,

L. Picas, S. Vassilopoulos, Caveolae and Bin1 form ring-shaped platforms for T-tubule initiation. *eLife* **12**, e84139 (2023).

39. M. Collot, P. Ashokkumar, H. Anton, E. Boutant, O. Faklaris, T. Galli, Y. Mély, L. Danglot, A. S. Klymchenko, MemBright: A Family of Fluorescent Membrane Probes for Advanced Cellular Imaging and Neuroscience. *Cell Chemical Biology* **26**, 600-614.e7 (2019).

40. S. Loebrich, The role of F-actin in modulating Clathrin-mediated endocytosis: Lessons from neurons in health and neuropsychiatric disorder. *Communicative & Integrative Biology* **7**, e28740 (2014).

41. R. Zhou, B. Han, C. Xia, X. Zhuang, Membrane-associated periodic skeleton is a signaling platform for RTK transactivation in neurons. *Science* **365**, 929–934 (2019).

42. K. L. Hedstrom, X. Xu, Y. Ogawa, R. Frischknecht, C. I. Seidenbecher, P. Shrager, M. N. Rasband, Neurofascin assembles a specialized extracellular matrix at the axon initial segment. *J Cell Biol* **178**, 875–886 (2007).

43. A. Brachet, C. Leterrier, M. Irondelle, M.-P. Fache, V. Racine, J.-B. Sibarita, D. Choquet, B. Dargent, Ankyrin G restricts ion channel diffusion at the axonal initial segment before the establishment of the diffusion barrier. *J Cell Biol* **191**, 383–395 (2010).

44. S. Tuvia, T. D. Garver, V. Bennett, The phosphorylation state of the FIGQY tyrosine of neurofascin determines ankyrin-binding activity and patterns of cell segregation. *Proc Natl Acad Sci U S A* **94**, 12957–12962 (1997).

45. A. Bréchet, M.-P. Fache, A. Brachet, G. Ferracci, A. Baude, M. Irondelle, S. Pereira, C. Leterrier, B. Dargent, Protein kinase CK2 contributes to the organization of sodium channels in axonal membranes by regulating their interactions with ankyrin G. *J Cell Biol* **183**, 1101–1114 (2008).

46. R. Yamada, H. Kuba, Structural and Functional Plasticity at the Axon Initial Segment. *Front Cell Neurosci* **10**, 250 (2016).

47. S. Kaech, G. Banker, Culturing hippocampal neurons. *Nat Protoc* **1**, 2406–2415 (2006).

48. A. Ganguly, R. Sharma, N. P. Boyer, F. Wernert, S. Phan, D. Boassa, L. Parra, U. Das, G. Caillol, X. Han, J. R. Yates, M. H. Ellisman, C. Leterrier, S. Roy, Clathrin packets move in slow axonal transport and deliver functional payloads to synapses. *Neuron* **109**, 2884-2901.e7 (2021).

49. M. A. Cousin, B. A. Creighton, K. A. Breau, R. C. Spillmann, E. Torti, S. Dontu, S. Tripathi, D. Ajit, R. J. Edwards, S. Afriyie, J. C. Bay, K. M. Harper, A. A. Beltran, L. J. Munoz, L. Falcon Rodriguez, M. C. Stankewich, R. E. Person, Y. Si, E. A. Normand, A. Blevins, A. S. May, L. Bier, V. Aggarwal, G. M. S. Mancini, M. A. van Slegtenhorst, K. Cremer, J. Becker, H. Engels, S. Aretz, J. J. MacKenzie, E. Brilstra, K. L. I. van Gassen, R. H. van Jaarsveld, R. Oegema, G. M. Parsons, P. Mark, I. Helbig, S. E. McKeown, R. Stratton, B. Cogne, B. Isidor, P. Cacheiro, D. Smedley, H. V. Firth, T. Bierhals, K. Kloth, D. Weiss, C. Fairley, J. T. Shieh, A. Kritzer, P. Jayakar, E. Kurtz-Nelson, R. A. Bernier, T. Wang, E. E. Eichler, I. M. B. H. van de Laar, A. McConkie-Rosell, M. T. McDonald, J. Kemppainen, B. C. Lanpher, L. E. Schultz-Rogers, L. B. Gunderson, P. N. Pichurin, G. Yoon, M. Zech, R. Jech, J. Winkelmann, A. S. Beltran, M. T. Zimmermann, B. Temple, S. S. Moy, E. W. Klee, Q. K.-G. Tan, D. N. Lorenzo, Q. K.-G. Tan, D. N. Lorenzo,

Pathogenic SPTBN1 variants cause an autosomal dominant neurodevelopmental syndrome. *Nat Genet* **53**, 1006–1021 (2021).

50. J.-Y. Jeong, H.-S. Yim, J.-Y. Ryu, H. S. Lee, J.-H. Lee, D.-S. Seen, S. G. Kang, One-step sequence- and ligation-independent cloning as a rapid and versatile cloning method for functional genomics studies. *Appl Environ Microbiol* **78**, 5440–5443 (2012).

51. M. R. Galiano, S. Jha, T. S.-Y. Ho, C. Zhang, Y. Ogawa, K.-J. Chang, M. C. Stankewich, P. J. Mohler, M. N. Rasband, A distal axonal cytoskeleton forms an intra-axonal boundary that controls axon initial segment assembly. *Cell* **149**, 1125–1139 (2012).

52. Y. Gao, E. Hisey, T. W. A. Bradshaw, E. Erata, W. E. Brown, J. L. Courtland, A. Uezu, Y. Xiang, Y. Diao, S. H. Soderling, Plug-and-Play Protein Modification Using Homology-Independent Universal Genome Engineering. *Neuron* **103**, 583-597.e8 (2019).

53. J. Heuser, The production of "cell cortices" for light and electron microscopy. *Traffic* **1**, 545–552 (2000).

54. A. Jimenez, K. Friedl, C. Leterrier, About samples, giving examples: Optimized Single Molecule Localization Microscopy. *Methods* **174**, 100–114 (2020).

55. A. Speiser, L.-R. Müller, P. Hoess, U. Matti, C. J. Obara, W. R. Legant, A. Kreshuk, J. H. Macke, J. Ries, S. C. Turaga, Deep learning enables fast and dense single-molecule localization with high accuracy. *Nat Methods* **18**, 1082–1090 (2021).

56. Y. Wang, J. Schnitzbauer, Z. Hu, X. Li, Y. Cheng, Z.-L. Huang, B. Huang, Localization events-based sample drift correction for localization microscopy with redundant cross-correlation algorithm. *Opt Express* **22**, 15982–15991 (2014).

57. J. Ries, SMAP: a modular super-resolution microscopy analysis platform for SMLM data. *Nat Methods* **17**, 870–872 (2020).

58. M. Ovesný, P. Křížek, J. Borkovec, Z. Švindrych, G. M. Hagen, ThunderSTORM: a comprehensive ImageJ plug-in for PALM and STORM data analysis and super-resolution imaging. *Bioinformatics* **30**, 2389–2390 (2014).

59. P. Paul-Gilloteaux, X. Heiligenstein, M. Belle, M.-C. Domart, B. Larijani, L. Collinson, G. Raposo, J. Salamero, eC-CLEM: flexible multidimensional registration software for correlative microscopies. *Nat Methods* **14**, 102–103 (2017).

60. J. Schindelin, I. Arganda-Carreras, E. Frise, V. Kaynig, M. Longair, T. Pietzsch, S. Preibisch, C. Rueden, S. Saalfeld, B. Schmid, J.-Y. Tinevez, D. J. White, V. Hartenstein, K. Eliceiri, P. Tomancak, A. Cardona, Fiji: an open-source platform for biological-image analysis. *Nat Methods* **9**, 676–682 (2012).

61. U. Schmidt, M. Weigert, C. Broaddus, G. Myers, "Cell Detection with Star-Convex Polygons" in *Medical Image Computing and Computer Assisted Intervention – MICCAI 2018*, A. F. Frangi, J. A. Schnabel, C. Davatzikos, C. Alberola-López, G. Fichtinger, Eds. (Springer International Publishing, Cham, 2018), pp. 265–273.

62. E. Meijering, M. Jacob, J.-C. F. Sarria, P. Steiner, H. Hirling, M. Unser, Design and validation of a tool for neurite tracing and analysis in fluorescence microscopy images. *Cytometry A* **58**, 167–176 (2004).

Acknowledgments: We would like to thank Subhojit Roy and Marc Bitoun for insightful discussions, as well as Damaris Lorenzo for the gift of the EGFP-ß2-spectrin plasmid.

Funding: We would like to acknowledge funding by the *Agence Nationale pour la Recherche* (ANR-20-CE13-0024-01 to CL and SV, ANR-21-CE13-0018-01 to SV), *Fédération pour la Recherche sur le Cerveau* (AOE 16 “Espoir en tête” 2021) to CL, Sorbonne Université, INSERM, Association Institut de Myologie core funding to SV. We would like to thank the Neuro-Cellular Imaging Service and Nikon Center for Neuro-NanoImaging at INP, with funding from CPER-FEDER (PlateForme NeuroTimone PA0014842), the Institut Marseille Imaging and NeuroMarseille for complementary equipment funding from Excellence Initiative of Aix-Marseille University – A*MIDEX, a French “Investissements d’Avenir” program (AMX-19-IET-002), and NeuroSchool for end-of-PhD funding. We would also like to thank the IBPS electron microscopy platform (Sorbonne University, Paris, France) and the MyoVector facility from the Institute of Myology (Paris, France)

Author contributions:

Conceptualization: CL, SV

Methodology: FW, SM, JL, NJ, CL, SV

Formal analysis: FW, SM, CL, SV

Investigation: FW, SM, FP, JL, ES, GM, FB-R, SB-Z, M-JP, CL, SV

Resources: NJ

Writing-Original Draft: SM, CL, SV

Writing-Review and Editing: FW, SM, JL, M-JP, CL, SV

Visualization: FW, SM, CL, SV

Supervision, Project Administration: CL, SV

Funding acquisition: CL, SV

Competing interests: All other authors declare they have no competing interests.

Data and materials availability: All data are available in the main text or the supplementary materials.

Supplementary Materials

Figs. S1 to S7

Movies S1 to S2

Data S1

Figure Legends

Fig. 1. Clathrin-coated pits are present in clearings of the periodic spectrin scaffold at the AIS.

(A) SIM image of a cultured hippocampal neuron at 14 days in vitro (div) fixed and stained for clathrin (magenta, CCPs appear as clusters), α2-spectrin (green, ~190 nm-spaced bands are visible) and neurofascin (blue, labels the AIS). Scale bars, 10 µm (left image), 2 µm (center column), 0.5 µm (zooms). **(B)** Left, average images centered on CCPs for 591 individual pits showing the distribution of clathrin (magenta on overlay) and α2-spectrin (green on overlay). Right, radial intensity profile corresponding to the average images on the left (gray arrow), showing how CCPs reside in an area devoid of α2-spectrin. Scale bar, 100 nm. **(C)** SIM image of a neuron unroofed, fixed and stained for clathrin (magenta, CCPs appear as clusters) and α2-spectrin (green). Central column shows zooms corresponding to the area highlighted in the left image, while square images on the right correspond to zooms on the areas highlighted in the central column. Scale bars, 10 µm (left image), 2 µm (center column), 0.5 µm (zooms). **(D)** Left, average images centered on CCPs for 562 individual pits showing the distribution of clathrin (magenta on overlay) and α2-spectrin (green on overlay). Right, radial intensity profile corresponding to the average images on the left (gray arrow), showing how CCPs reside in an area devoid of α2-spectrin. Scale bar, 100 nm. **(E)** PREM view of an unroofed proximal axon showing the presence of microtubules (blue), ~190 nm-spaced actin rings (yellow), the dense mesh of spectrins between actin rings, and CCPs that reside in "clearings" of the spectrin mesh. Right images show zooms of square areas highlighted on the left image corresponding to an actin rings-spectrin mesh area, and an area with two CCPs. Scale bars, 200 nm (left image), 100 nm (zooms). **(F)** Gallery of PREM views showing CCPs found in circular areas of bare plasma membrane devoid of spectrin mesh ("clearings") along the proximal axon. Arrowheads point to isolated actin filaments contacting CCPs. Scale bars, 100 nm. **(G)** Quantification of the diameter for spectrin mesh clearings and for CCPs from PREM views. For all graphs unless stated otherwise, plots are individual points, bars are mean ± SEM, and significance are against the control condition (see Statistics section of the Material and Methods for details). All means, SEM and standard deviations together with statistics (number of points n, number of independent experiments N, significance of differences) are summarized in the Data S1 supplemental file.

Fig. 2. Molecular architecture of CCPs and actin-spectrin clearings at the AIS.

(A) Gallery of PREM views showing actin-spectrin mesh clearings at different stages of CCP formation, from empty clearing to clearing containing a nascent, single mature or multiple mature CCPs (left to right). Scale bars, 100 nm. **(B)** Quantification of the clearings diameter for empty clearing or clearings containing nascent, single or multiple CCPs. The percentage of clearings identified for each category is indicated above each bar. **(C)** Widefield image of a neuron fixed and stained for neurofascin (blue). The contour of the whole neuron (gray) is delineated. Scale bar, 10 µm. **(D)** 2-color 3D-PAINT images of the AIS corresponding to the image in B with staining for clathrin (magenta) and α2-spectrin (green). Scale bar, 2 µm. **(E)** Zooms showing individual CCPs (magenta) in clearing of the periodic α2-spectrin mesh (green) on XY images (top row, corresponding to areas highlighted in C) and corresponding XZ transverse sections (bottom row, taken between the lines highlighted on the XY images). Scale bars, 0.5 µm. **(F)** Correlative STORM-PREM image of an unroofed AIS labeled for ß4-spectrin (orange). Right, zoomed images showing CCPs in spectrin mesh clearings, with spectrin encircling the bare membrane area. **(G)** PREM view of an unroofed AIS immunogold-labeled for ß4-spectrin (yellow). Right, zoomed images showing CCPs in spectrin mesh clearings, with 15 nm gold beads bound to the spectrin mesh around the bare membrane area. **(H)** Correlative STORM-PREM image of an unroofed AIS labeled for actin (orange). Right, zoomed images showing CCPs in spectrin mesh clearings. Scale bars for E to G: 5 µm (left image), 100 nm (zooms). **(I)** Images of individual CCP-containing clearings from unroofed neurons stained for actin (orange) and imaged by correlative STORM-PREM. Scale bars, 100 nm.

Fig. 3. The submembrane actin-spectrin mesh restricts CCP formation at the AIS

(A) PREM views of the unroofed proximal axon of neurons infected with AAVs expressing control shRNAs (left) or targeted against α2-spectrin (middle left), ß4-spectrin (middle right) or α2-spectrin and ß4-spectrin (right), with CCPs colored in magenta on the main image. Insets are zooms of the area highlighted on the main images. Scale bars, 1 µm (main images), 200 nm (insets). **(B)** Effect of spectrins knockdown on the CCP density as quantified from PREM views of unroofed proximal axons. **(C)** Quantification of the submembrane organization (organized mesh, brown; disorganized mesh, gray; bare plasma membrane, purple) from PREM views of neurons in the control or shRNA against α2-spectrin conditions. **(D)** Effect of the treatment with vehicle (0.1% DMSO, 3h), Pitstop 2 (30 µM, 45 min), swinholide A (100 nM, 3h), or diamide (5 mM, 45 min) on the density of CCPs along the AIS as quantified from SIM images of intact neurons. **(E)** Effect of drug treatments on the density of CCPs along the AIS as quantified from SIM images of unroofed neurons. **(F)** SIM images of the proximal axon of neurons treated with drugs, fixed and stained for clathrin (magenta on overlay) and α2-spectrin (green on overlay). Scale bars, 5 µm. **(G)** SIM images of the proximal axon of neurons treated with drugs, then unroofed and fixed before being stained for clathrin (magenta on overlay) and α2-spectrin (green on overlay). Scale bars, 5 µm. **(H)** PREM views of the proximal axon of unroofed neurons after treatment with vehicle (DMSO 0.1%), Pitstop 2 (30 µM, 15 min), swinholide A (100 nM, 3h), or diamide (5 mM, 15 min), with CCPs colored in magenta on the main image. Zoomed insets correspond to the area highlighted on the main image. Scale bars, 1 µm (low-magnification image for diamide), 500 nm (main images), 200 nm (insets). **(I)** Effect of drugs on the density of CCPs along the AIS as quantified from PREM views of unroofed neurons. **(J)** Quantification of the submembrane organization (organized mesh, brown; disorganized mesh, gray; bare plasma membrane, purple) from PREM views of neurons in the control or drug-treated conditions.

Fig. 4. Endocytic cargo concentrates in stalled CCPs at the surface of the AIS

(A) SIM image of a neuron fed for 1h with transferrin-Alexa Fluor 647 (100 µg/mL, orange), fixed, and stained for map2 (dendrites, blue) and ß4-spectrin (AIS, green). Images on the right are straightened zooms along the dendrites and axon highlighted on the main image. **(B)** SIM image of a neuron fed for 30 min with dextran-Alexa Fluor 555 (50 µg/mL, orange), fixed, and stained for map2 (dendrites, blue) and ß4-spectrin (AIS, green). Images on the right are straightened zooms along the dendrites and axon highlighted on the main image. On A and B, dashed lines highlight the position of the AIS in the dextran uptake and clathrin channels. Scale bars on A and B: 10 µm (main image), 2 µm (zooms). **(C)** Left, SIM image of the AIS of a neuron fed with dextran-AF555 (30 min, yellow), fixed, and stained for clathrin (magenta) and neurofascin (blue). Some dextran clusters colocalize with CCPs (arrowheads). Right, average images of 591 pits centered on CCPs showing the distribution of dextran (orange), clathrin (magenta) and α2-spectrin (green). The graph shows the radial intensity profile corresponding to the average images, with the dextran clusters colocalizing with CCPs in an area devoid of α2-spectrin. **(D)** Left, SIM image of the AIS of a neuron fed with dextran-AF555 (yellow), unroofed, fixed, and stained for clathrin (magenta) and neurofascin (blue). Most dextran clusters colocalize with CCPs (arrowheads). Right, average images of 562 pits centered on CCPs showing the distribution of dextran (orange), clathrin (magenta) and α2-spectrin (green). The graph shows the radial intensity profile corresponding to the average images (gray arrow), with dextran cluster colocalizing with CCPs in an area devoid of α2-spectrin. Scale bars for C and D: 2 µm (AIS images), 1 µm (zooms), 100 nm (average images). **(E)** Correlative SIM-PREM image of the AIS of a neuron fed with dextran-AF555 (orange), unroofed, fixed, and stained for ß4-spectrin (green) and actin (blue). Zoomed overlays on the right show dextran clusters found at

CCPs in areas devoid of spectrin labeling (arrowheads). Scale bars, 5 µm (isolated SIM channels), 500 nm (main overlay), 100 nm (zooms). **(F)** SIM images of the AIS of neurons treated with vehicle (0.1% DMSO, 3h), Pitstop 2 (30 µM, 45 min), swinholide A (100 nM, 3h), or diamide (5 mM, 45 min), fed with dextran-AF555 (30 min, yellow), fixed, and stained for clathrin (magenta) and neurofascin (blue). Dashed lines highlight the position of the AIS in the dextran uptake and clathrin channels. Scale bars, 5 µm. **(G)** Effect of drugs on the density of dextran cluster density along the AIS as quantified from SIM images of intact neurons. **(H)** SIM images of the AIS of neurons treated with vehicle, Pitstop 2, swinholide A, and diamide, fed with dextran-AF555 (yellow), unroofed, fixed, and stained for clathrin (magenta) and neurofascin (blue). Dashed lines highlight the position of the AIS in the dextran uptake and clathrin channels. Scale bars, 5 µm. **(I)** Effect of drugs on the density of dextran clusters along the AIS as quantified from SIM images of unroofed neurons.

Fig. 5. Live-cell super-resolution microscopy reveals static CCPs along the AIS and proximal axon.

(A) Individual frame from Supplementary Movie 1 showing a neuron transfected with ß2spectrin-GFP (blue) and CLC-mCh (orange) and imaged by TIRF-SIM every 20s for 20 min. Scale bar, 5 µm. **(B)** Zooms on areas highlighted in A, with corresponding kymographs (highlighted white lines) along the AIS and proximal axon (top), along a dendrite (bottom left), inside the cell body (bottom center) and a neighboring glial cell (bottom right). Spectrin bands appear as vertical lines spaced by 190 nanometers in blue, while static pits appear as vertical lines and dynamic pits as dots in orange. Scale bars, 2 µm (images), 1 µm (kymograph horizontal), 5 min (kymograph vertical). **(C)** Time color-coded projection of the CLC-mCh channel for the neuronal compartments shown in the panels of B: static pits appear white, while dynamic pits are colored due to their transient appearance. Scale bars, 2 µm. **(D)** Temporal autocorrelation of the clathrin dynamics from tracings within the different compartments of neurons: AIS (orange), dendrites, and cell body. Significances corresponds to tests at 60,120, 180 and 240s (see Data S1). **(E)** Individual frame from Supplementary Movie 2 showing a neuron with CLC endogenously tagged with GFP (orange), and extracellular staining for neurofascin highlighting the AIS (blue), imaged by SoRa spinning disk every 5s for 10 min. Scale bar, 10 µm. **(F)** Zooms on areas highlighted in E, with corresponding kymographs (highlighted white lines) along the AIS (top left), along two dendrites (top and bottom right), and inside the cell body (bottom left). Static CCPs appear as vertical lines, with putative endocytic events appearing as discontinuities of characteristic J-shaped traces. Scale bars, 2 µm (image), 1 µm (kymograph horizontal), 5 min (kymograph vertical). (**G)** Time color-coded projection of CLC-GFP for the neuronal compartments shown in the panels of B: static pits appear white, while dynamic pits are colored due to their transient appearance. Scale bars, 2 µm. (**H)** Temporal autocorrelation of the clathrin dynamics from tracings within the different compartments of neurons, showing the relative stability of CLC in the axon (orange) compared to the dendrites (blue,) and cell body (magenta). Significances corresponds to tests at 60,120, 180 and 240s (see Data S1).

Fig. 6. Endocytosis at the AIS can be triggered by plasticity-inducing stimulation.

(A) SIM images of the AIS of neurons treated with vehicle (0.1% water), or NMDA (50 µM, 4 min followed by 30 min rest), fed with dextran-AF555 (30 min, yellow), fixed, and stained for clathrin (magenta) and neurofascin (blue). **(B)** SIM images of the AIS of neurons treated with vehicle (0.1% DMSO), or NMDA, fed with dextran-AF555 (yellow), unroofed, fixed, and stained for clathrin (magenta) and neurofascin (blue). On A and B, dashed lines highlight the position of the AIS in the dextran uptake and clathrin channels. Scale bars for A and B, 5 µm. **(C)** Effect of NMDA stimulation on the CCP density along the AIS as quantified from SIM images of intact neurons (left graphs) or unroofed neurons (right graph). **(D)** Effect of NMDA stimulation on the dextran cluster density along the AIS as quantified from SIM images of intact neurons (left graphs) or unroofed neurons (right graph). **(E)** SIM images of neurons treated with vehicle or NMDA, fed 30 min with MemGlow560 (gray) and anti-neurofascin extracellular antibody (blue), fixed and stained. Scale bars, 5 µm (main images), 1 µm (zooms). **(F)** PREM views of the proximal axon of unroofed neurons after treatment with vehicle, NMDA, or NMDA+LatA (5 µM throughout the experiment) with CCPs colored in magenta and branched actin surrounding CCPs colored in yellow on the main image. Zooms corresponds to the area highlighted on the main image. Scale bars, 1 µm (main images), 200 nm (zooms). **(G)** Surface occupied by branched actin inside clearings in the control, NMDA and NMDA+LatA conditions. **(H)**. SIM images of the AIS of neurons treated with vehicle, NMDA or NMDA+LatA, unroofed, fixed, and stained for actin (gray), clathrin (orange) and ß4-spectrin (blue). Arrowheads point to actin clusters apposed to CCPs. Scale bars, 5 µm (main images), 1 µm (zooms). **(I)**. CCP density quantified from PREM views of unroofed neurons treated with vehicle or NMDA. **(J)** average number of CCPs per clearing quantified from PREM views of unroofed neurons treated with vehicle or NMDA. **(K)** SIM images of the AIS of neurons treated with vehicle (0.1% water), NMDA (50 µm, 4 min followed by 30 min rest), or NMDA+LatA (5 µM throughout the experiment), fed with dextran-AF555 (30 min, yellow), fixed, and stained for clathrin (magenta) and neurofascin (blue). Dashed lines highlight the position of the AIS in the dextran uptake and clathrin channels. Scale bars, 5 µm. **(L)** CCP density along the AIS of neurons treated with vehicle, NMDA, or NMDA+LatA as quantified from SIM images of intact neurons. **(M)** Dextran cluster density along the AIS of neurons treated with vehicle, NMDA, or NMDA+LatA as quantified from SIM images of intact neurons.

Figure 1

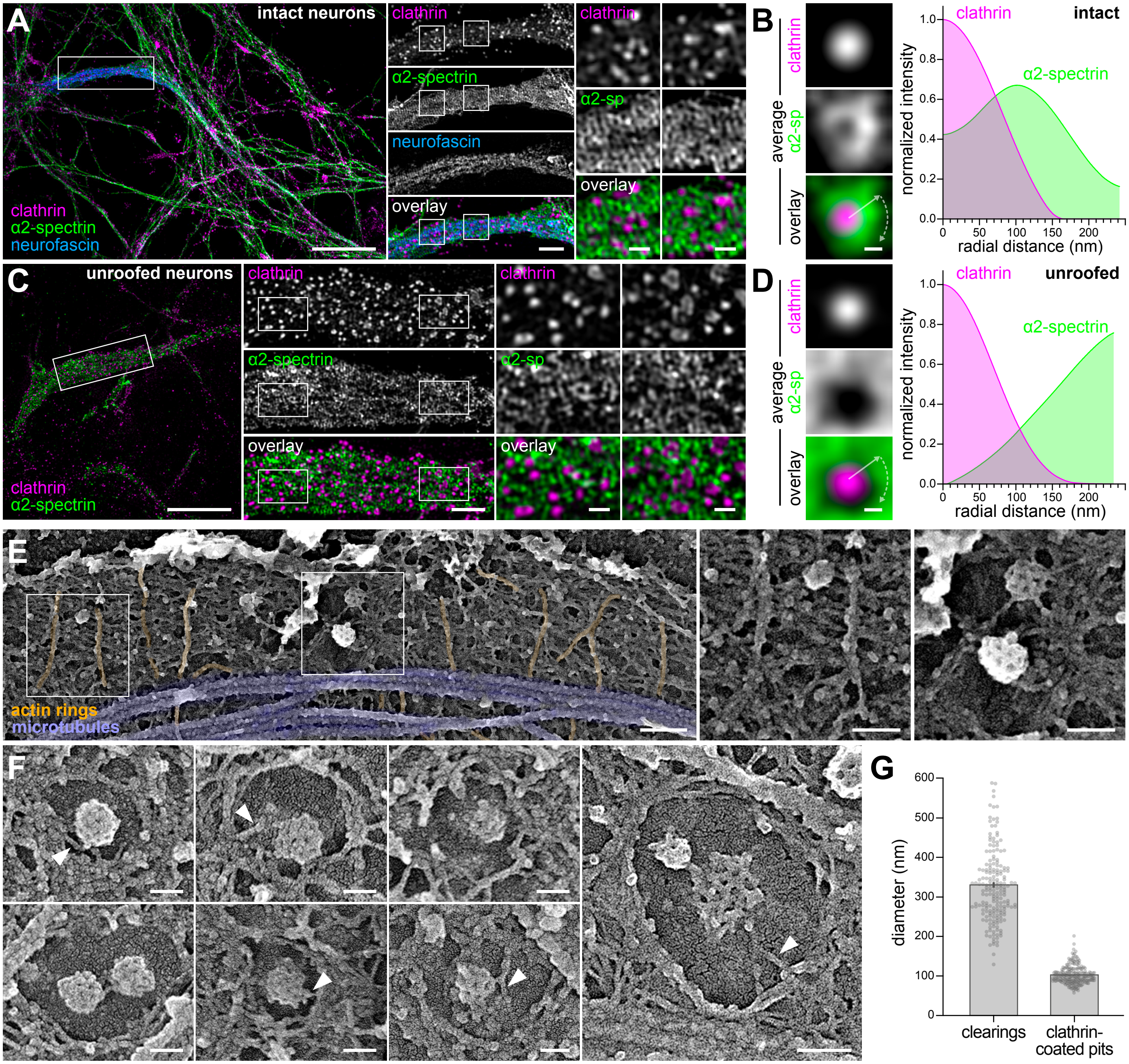
A
intact neurons
clathrin
α2-spectrin
neurofascin
clathrin
α2-spectrin
neurofascin
overlay
clathrin
α2-sp
overlay
B
average
clathrin
α2-sp
overlay
clathrin
intact
α2-spectrin
normalized intensity
1.0
0.8
0.6
0.4
0.2
0.0
0
50
100
150
200
radial distance (nm)
C
unroofed neurons
clathrin
α2-spectrin
clathrin
α2-spectrin
overlay
clathrin
α2-sp
overlay
D
average
clathrin
α2-sp
overlay
clathrin
unroofed
α2-spectrin
normalized intensity
1.0
0.8
0.6
0.4
0.2
0.0
0
50
100
150
200
radial distance (nm)
E
actin rings
microtubules
F
G
diameter (nm)
600
500
400
300
200
100
0
clearings
clathrin-coated pits

Figure 2

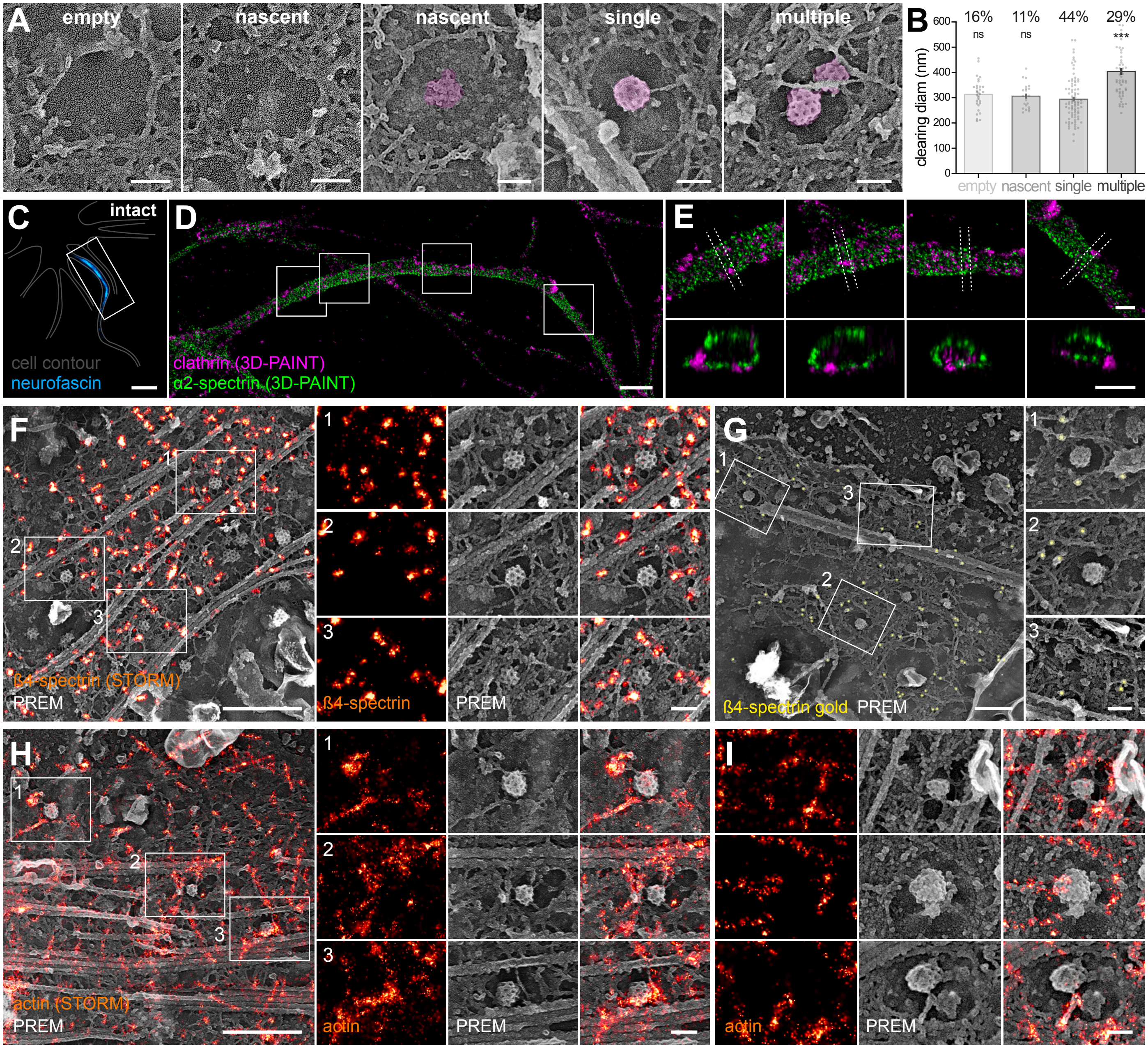
A
empty
nascent
nascent
single
multiple
B
16%
11%
44%
29%
ns
ns
***
clearing diam (nm)
0
100
200
300
400
500
600
empty
nascent
single
multiple
C
intact
cell contour
neurofascin
D
clathrin (3D-PAINT)
α2-spectrin (3D-PAINT)
E
F
1
2
3
ß4-spectrin (STORM)
PREM
ß4-spectrin
PREM
G
1
2
3
ß4-spectrin gold
PREM
H
1
2
3
actin (STORM)
PREM
actin
PREM
I
actin
PREM

Figure 3

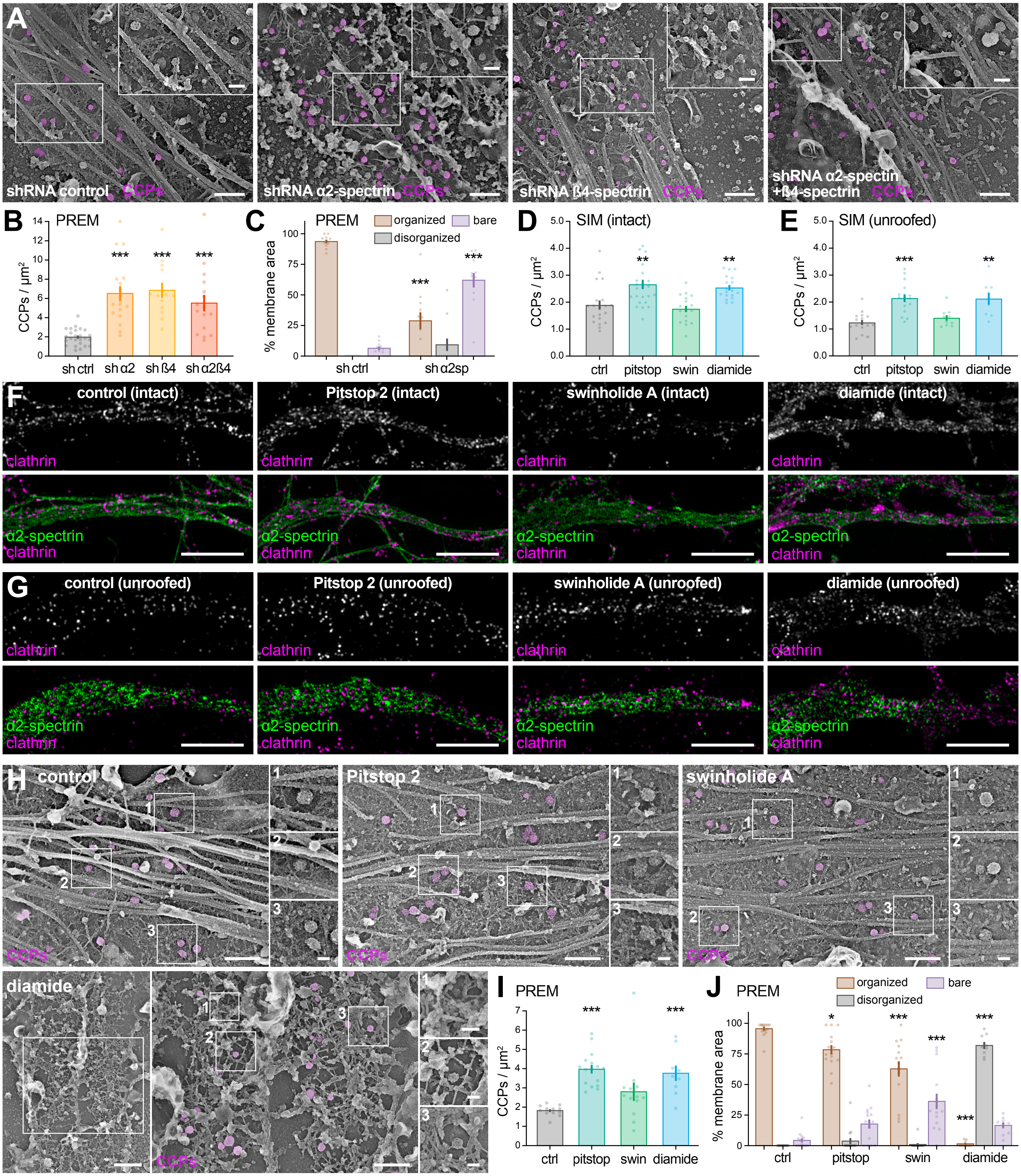
A
shRNA control CCPs
shRNA α2-spectrin CCPs
shRNA ß4-spectrin CCPs
shRNA α2-spectin +ß4-spectrin CCPs
B PREM
CCPs / µm²
0 2 4 6 8 10 12 14
***
***
***
sh ctrl
sh α2
sh ß4
sh α2ß4
C PREM
organized
bare
disorganized
% membrane area
0 25 50 75 100
***
***
sh ctrl
sh α2sp
D SIM (intact)
CCPs / µm²
0.0 1.0 2.0 3.0 4.0 5.0
**
**
ctrl pitstop swin diamide
E SIM (unroofed)
CCPs / µm²
0.0 1.0 2.0 3.0 4.0 5.0
***
**
ctrl pitstop swin diamide
F
control (intact)
Pitstop 2 (intact)
swinholide A (intact)
diamide (intact)
clathrin
α2-spectrin
clathrin
G
control (unroofed)
Pitstop 2 (unroofed)
swinholide A (unroofed)
diamide (unroofed)
clathrin
α2-spectrin
clathrin
H
control
Pitstop 2
swinholide A
diamide
1 2 3
CCPs
I PREM
CCPs / µm²
0 1 2 3 4 5 6 7
***
***
ctrl pitstop swin diamide
J PREM
organized
bare
disorganized
% membrane area
0 25 50 75 100
*
***
***
***
***
ctrl pitstop swin diamide

Figure 4

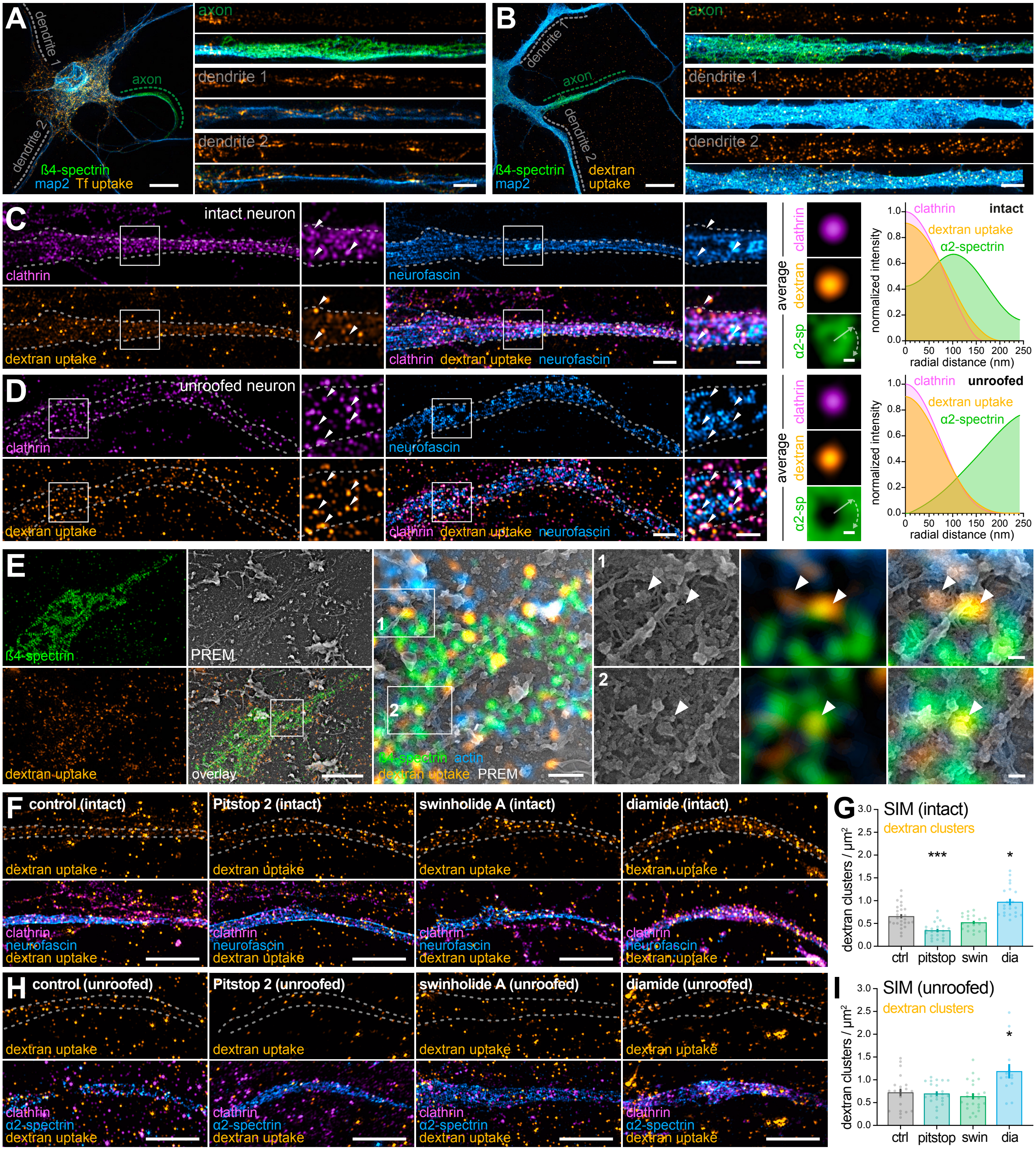
A
dendrite 1
axon
dendrite 2
ß4-spectrin
map2 Tf uptake
axon
dendrite 1
dendrite 2
B
dendrite 1
axon
dendrite 2
ß4-spectrin
map2
dextran
uptake
axon
dendrite 1
dendrite 2
C
intact neuron
clathrin
dextran uptake
neurofascin
clathrin dextran uptake neurofascin
average
clathrin
dextran
α2-sp
clathrin
intact
dextran uptake
α2-spectrin
normalized intensity
1.0
0.8
0.6
0.4
0.2
0.0
0 50 100 150 200 250
radial distance (nm)
D
unroofed neuron
clathrin
dextran uptake
neurofascin
clathrin dextran uptake neurofascin
average
clathrin
dextran
α2-sp
clathrin
unroofed
dextran uptake
α2-spectrin
normalized intensity
1.0
0.8
0.6
0.4
0.2
0.0
0 50 100 150 200 250
radial distance (nm)
E
ß4-spectrin
PREM
dextran uptake
overlay
1
2
ß4-spectrin actin
dextran uptake PREM
1
2
F
control (intact)
Pitstop 2 (intact)
swinholide A (intact)
diamide (intact)
dextran uptake
clathrin
neurofascin
dextran uptake
G
SIM (intact)
dextran clusters
dextran clusters / µm²
3.0
2.5
2.0
1.5
1.0
0.5
0.0
***
*
ctrl pitstop swin dia
H
control (unroofed)
Pitstop 2 (unroofed)
swinholide A (unroofed)
diamide (unroofed)
dextran uptake
clathrin
α2-spectrin
dextran uptake
I
SIM (unroofed)
dextran clusters
dextran clusters / µm²
3.0
2.5
2.0
1.5
1.0
0.5
0.0
*
ctrl pitstop swin dia

Figure 5

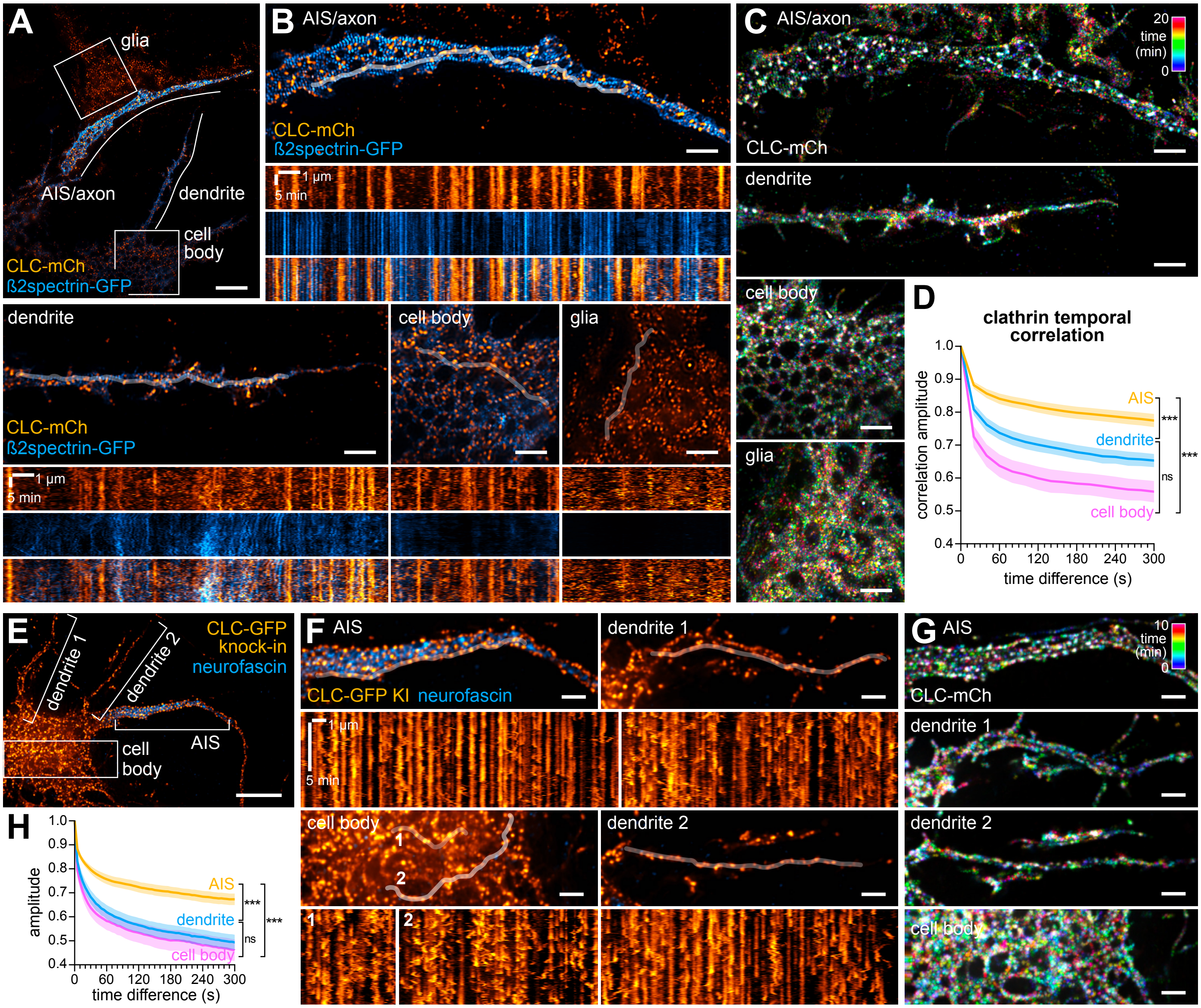
A
glia
AIS/axon
dendrite
cell body
CLC-mCh
ß2spectrin-GFP
B
AIS/axon
CLC-mCh
ß2spectrin-GFP
1 µm
5 min
dendrite
cell body
glia
CLC-mCh
ß2spectrin-GFP
1 µm
5 min
C
AIS/axon
20
time (min)
0
CLC-mCh
dendrite
cell body
glia
D
clathrin temporal correlation
correlation amplitude
1.0
0.9
0.8
0.7
0.6
0.5
0.4
0
60
120
180
240
300
time difference (s)
AIS
dendrite
cell body
***
***
ns
E
CLC-GFP knock-in
neurofascin
dendrite 1
dendrite 2
cell body
AIS
F
AIS
CLC-GFP KI
neurofascin
dendrite 1
1 µm
5 min
cell body
1
2
dendrite 2
1
2
G
AIS
10
time (min)
0
CLC-mCh
dendrite 1
dendrite 2
cell body
H
amplitude
1.0
0.9
0.8
0.7
0.6
0.5
0.4
0
60
120
180
240
300
time difference (s)
AIS
dendrite
cell body
***
***
ns

Figure 6

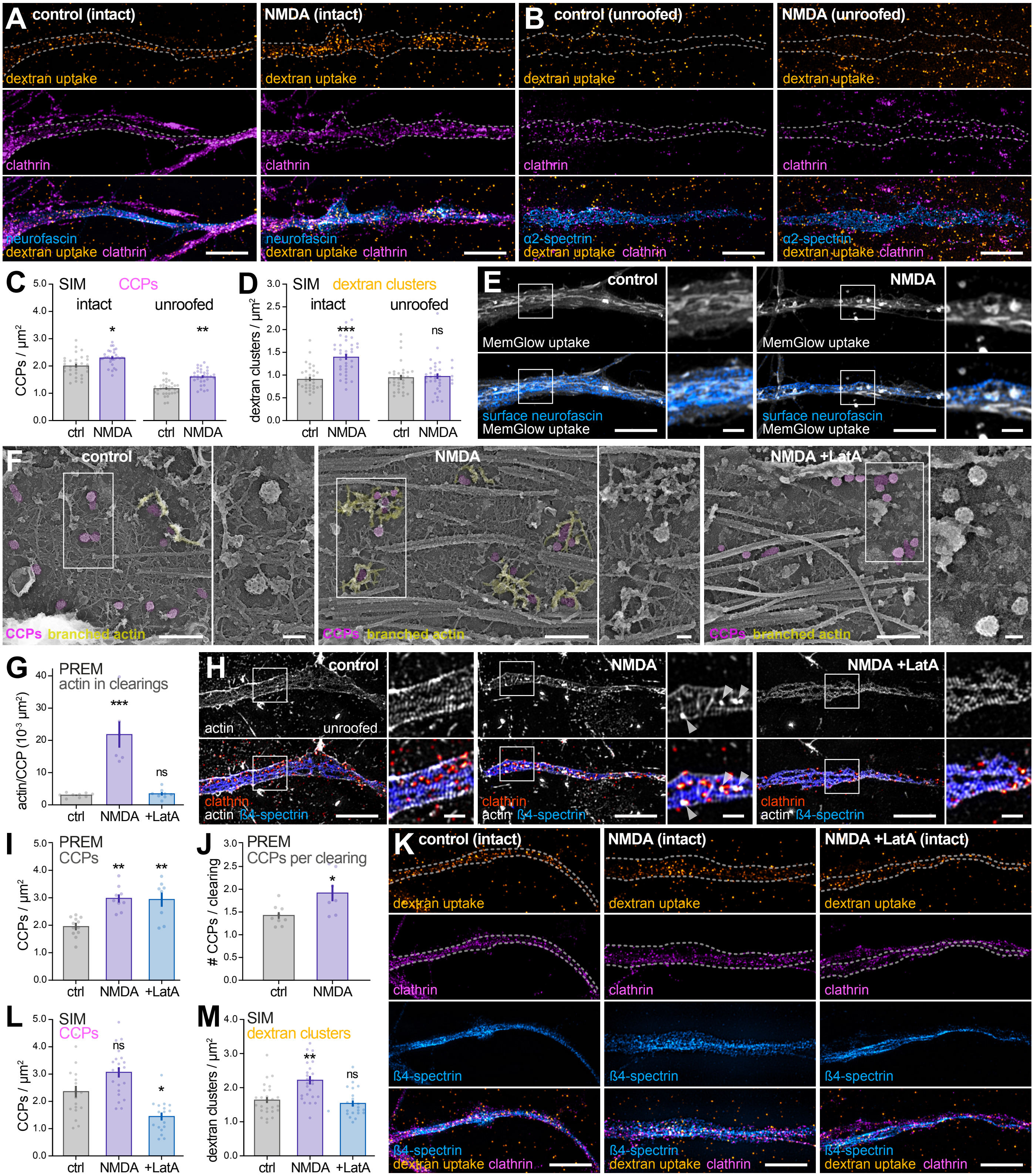
A
control (intact)
NMDA (intact)
dextran uptake
clathrin
neurofascin
dextran uptake clathrin
B
control (unroofed)
NMDA (unroofed)
dextran uptake
clathrin
α2-spectrin
dextran uptake clathrin
C
SIM
CCPs
intact
unroofed
CCPs / µm²
5.0
4.0
3.0
2.0
1.0
0.0
*
**
ctrl
NMDA
ctrl
NMDA
D
SIM
dextran clusters
intact
unroofed
dextran clusters / µm²
3.0
2.5
2.0
1.5
1.0
0.5
0.0
***
ns
ctrl
NMDA
ctrl
NMDA
E
control
NMDA
MemGlow uptake
surface neurofascin
MemGlow uptake
F
control
NMDA
NMDA +LatA
CCPs
branched actin
G
PREM
actin in clearings
actin/CCP (10⁻³ µm²)
40
30
20
10
0
***
ns
ctrl
NMDA
+LatA
H
control
NMDA
NMDA +LatA
actin
unroofed
clathrin
actin
ß4-spectrin
I
PREM
CCPs
CCPs / µm²
5.0
4.0
3.0
2.0
1.0
0.0
**
**
ctrl
NMDA
+LatA
J
PREM
CCPs per clearing
CCPs / clearing
3.0
2.5
2.0
1.5
1.0
0.5
0.0
*
ctrl
NMDA
K
control (intact)
NMDA (intact)
NMDA +LatA (intact)
dextran uptake
clathrin
ß4-spectrin
ß4-spectrin
dextran uptake clathrin
L
SIM
CCPs
CCPs / µm²
5.0
4.0
3.0
2.0
1.0
0.0
ns
*
ctrl
NMDA
+LatA
M
SIM
dextran clusters
dextran clusters / µm²
4.0
3.0
2.0
1.0
0.0
**
ns
ctrl
NMDA
+LatA

Supplementary Materials for

The actin-spectrin submembrane scaffold restricts endocytosis along proximal axons

Florian Wernert, Satish Moparthi *et al.*

Corresponding authors: christophe.leterrier@univ-amu.fr and s.vassilopoulos@institut-myologie.org

The PDF file includes:

Figs. S1 to S7
Captions for Movie S1 to S2
Captions for Data S1

Other Supplementary Materials for this manuscript include the following:

Movies S1 to S2
Data S1

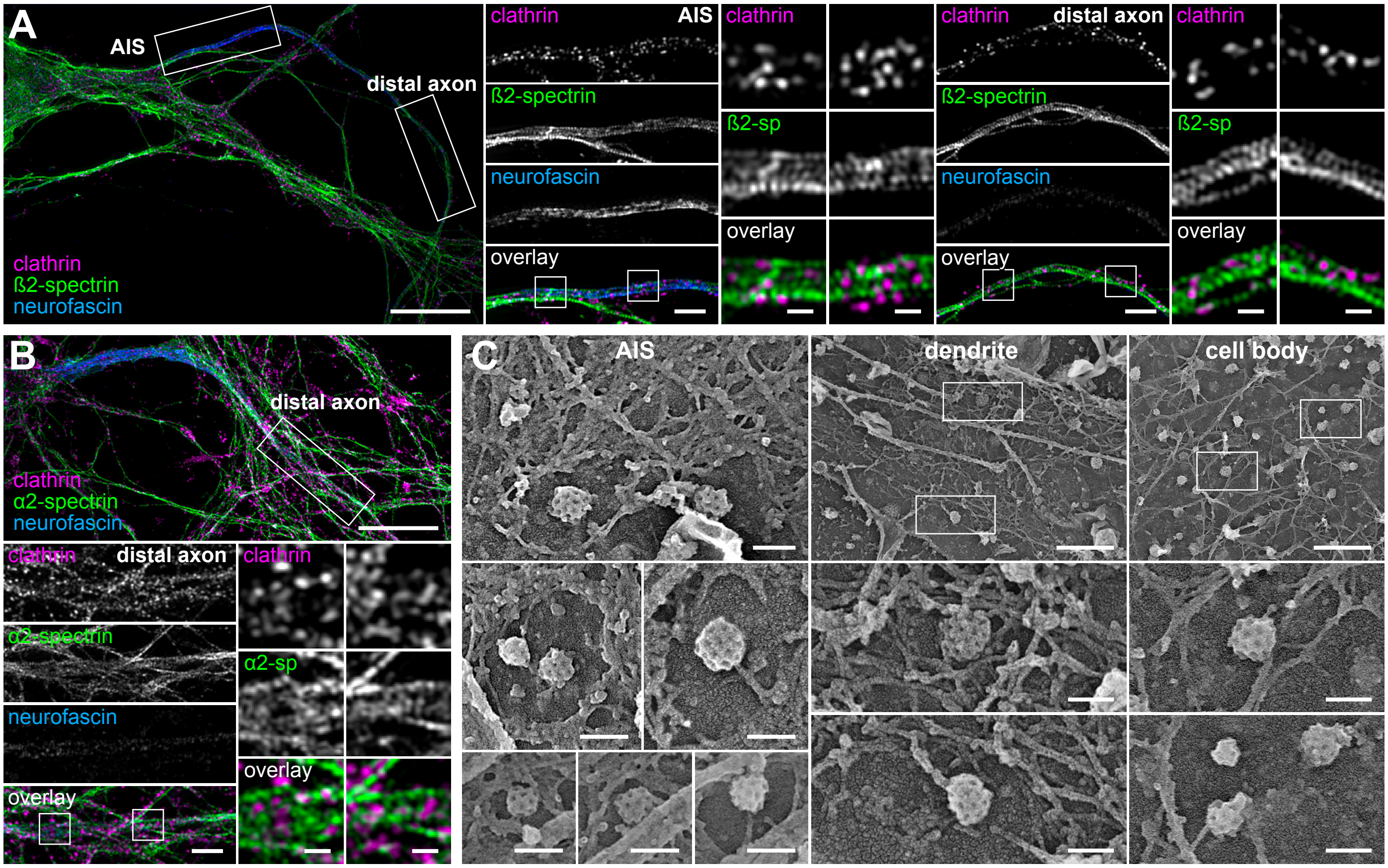

Fig. S1: Clearings of the periodic spectrin mesh encase CCPs along the AIS and distal axon, but not in the dendrites or cell body of neurons.
(A) SIM image of a cultured hippocampal neuron at 14 div fixed and stained for clathrin (magenta, pits appear as clusters), ß2-spectrin (green, ~190 nm-spaced bands are visible) and neurofascin (blue, labels the AIS). Zooms show portions of the AIS (center panels) and distal axon after the AIS (right panels). Scale bars, 10 µm (left image), 2 µm (center column), 0.5 µm (square zoomed images). (**B**) Same SIM image as in Fig. 1A of a cultured hippocampal neuron at 14 div fixed and stained for clathrin (magenta), α2-spectrin (green) and neurofascin (blue), with a zoom on the distal axon (bottom panels). Scale bars, 10 µm (top image), 2 µm (bottom left panels), 0.5 µm (bottom right square zoomed images). (**C**) Left, PREM views showing CCPs found along the AIS in circular areas devoid of the actin-spectrin scaffold (left), or along dendrites (center) and in the cell body (right) where the submembrane scaffold is sparser. Scale bars, 100 nm.

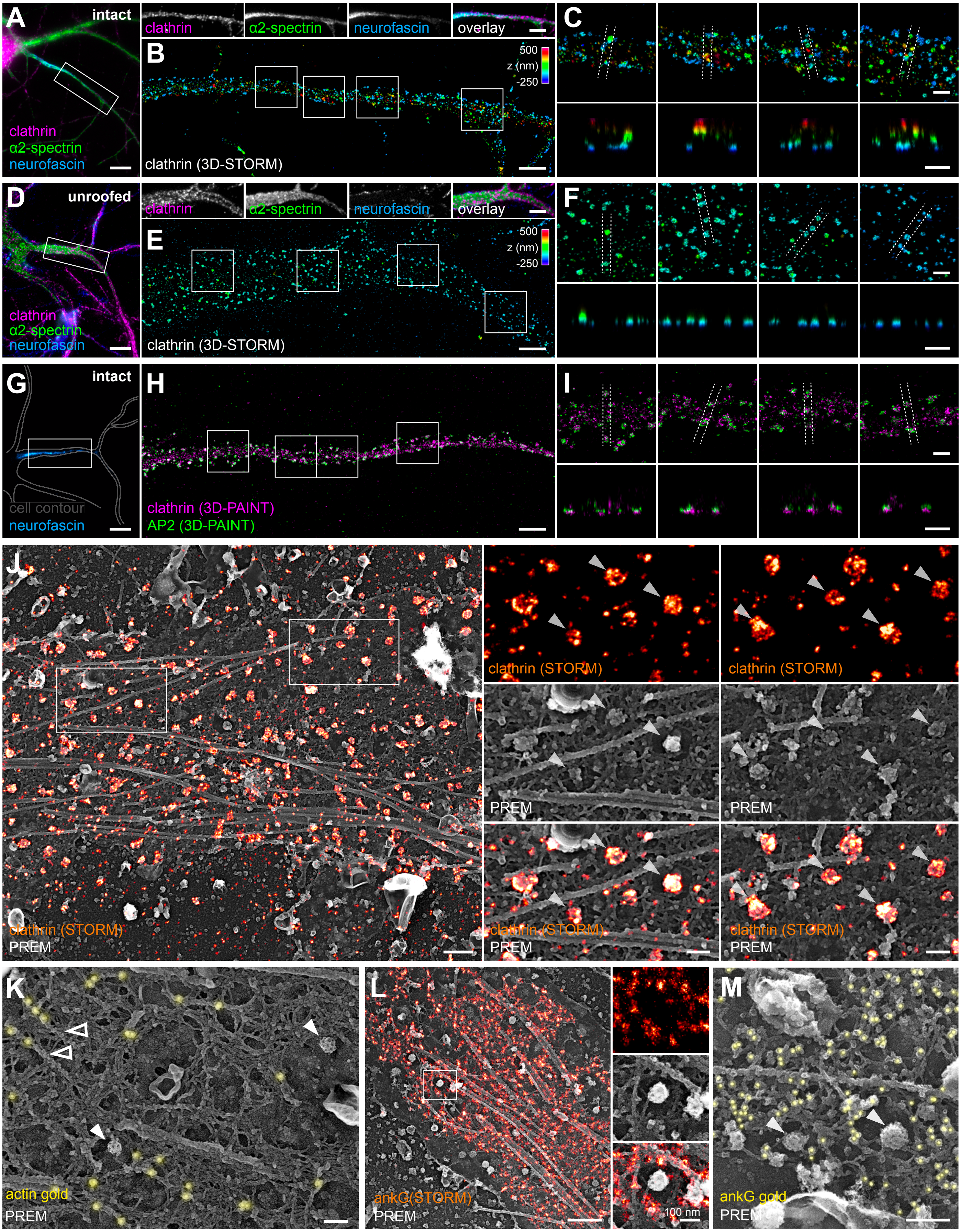
A
intact
clathrin
α2-spectrin
neurofascin
overlay
B
500
z (nm)
-250
clathrin (3D-STORM)
C
D
unroofed
clathrin
α2-spectrin
neurofascin
overlay
E
500
z (nm)
-250
clathrin (3D-STORM)
F
G
intact
cell contour
neurofascin
H
clathrin (3D-PAINT)
AP2 (3D-PAINT)
I
J
clathrin (STORM)
PREM
K
actin gold
PREM
L
ankG (STORM)
PREM
100 nm
M
ankG gold
PREM

Fig. S2. Molecular organization of CCPs, ankyrin G and pMLC along AIS. *(See Figure on previous page)*
(A) Widefield image of a neuron fixed and stained for clathrin (magenta), α2-spectrin (green) and neurofascin (blue). Line of images on top right are individual channels and overlays corresponding to the AIS area highlighted on the left image. Scale bars, 10 µm (left image), 5 µm (AIS images). (**B)** 3D-STORM image of clathrin corresponding to the AIS area shown in A, color coded for depth. Scale bar, 2 µm. (**C)** Zooms showing individual CCPs on XY images (top row, corresponding to areas highlighted in B) and corresponding XZ transverse sections (bottom row, taken between the lines highlighted on the XY images). Pits are mostly found at the plasma membrane, delineating the axon contour on transverse sections. Scale bars, 0.5 µm. **(D)** Widefield image of a neuron unroofed, fixed and stained for clathrin (magenta), α2-spectrin (green) and neurofascin (blue). Line of images on top right are individual channels and overlays corresponding to the AIS area highlighted on the left image. Scale bars, 10 µm (left image), 5 µm (AIS images). (**E)** 3D-STORM image of clathrin corresponding to the AIS area shown in D, color coded for depth. Scale bar, 2 µm. (**F)** Zooms showing individual CCPs on XY images (top row, corresponding to areas highlighted in E) and corresponding XZ transverse sections (bottom row, taken between the lines highlighted on the XY images). Pits are found along the remaining ventral plasma membrane after unroofing. Scale bars, 0.5 µm. (**G)** Widefield image of a neuron fixed and stained for neurofascin (blue). The contour of the whole neuron is delineated (gray). Scale bar, 10 µm. (**H)** 2-color 3D-PAINT images of the AIS corresponding to the image in G with staining for clathrin (magenta) and AP2 (green). Scale bar, 2 µm. (**I)** Zooms showing individual CCPs immunolabeled for clathrin heavy chain (magenta) and AP2 (green) on XY images (top row, corresponding to areas highlighted in H) and corresponding XZ transverse sections (bottom row, taken between the lines highlighted on the XY images). Both clathrin and AP2 colocalize at CCPs. Scale bars, 0.5 µm. (**J)** Correlative STORM-PREM image of an unroofed AIS immunolabeled for clathrin (orange). Right, zoomed images showing CCPs in spectrin mesh clearings (arrowheads). Scale bars, 500 nm (left image), 100 nm (zooms). **(K)** PREM view of an unroofed AIS immunogold-labeled for actin (yellow) showing CCPs in spectrin mesh clearings (arrowheads), with 15 nm gold beads bound to actin rings (see the ~200-nm spacing at top left, empty arrowheads). Scale bar, 100 nm. (**L)** Correlative STORM-PREM image of an unroofed AIS immunolabeled for ankyrin G (ankG, orange). Right, zoomed images showing CCPs in spectrin mesh clearings. Scale bars, 500 nm (left image), 100 nm (zooms). **(M)** PREM view of an unroofed AIS immunogold-labeled for ankG (yellow) showing CCPs in spectrin mesh clearings (arrowheads). Scale bar, 200 nm.

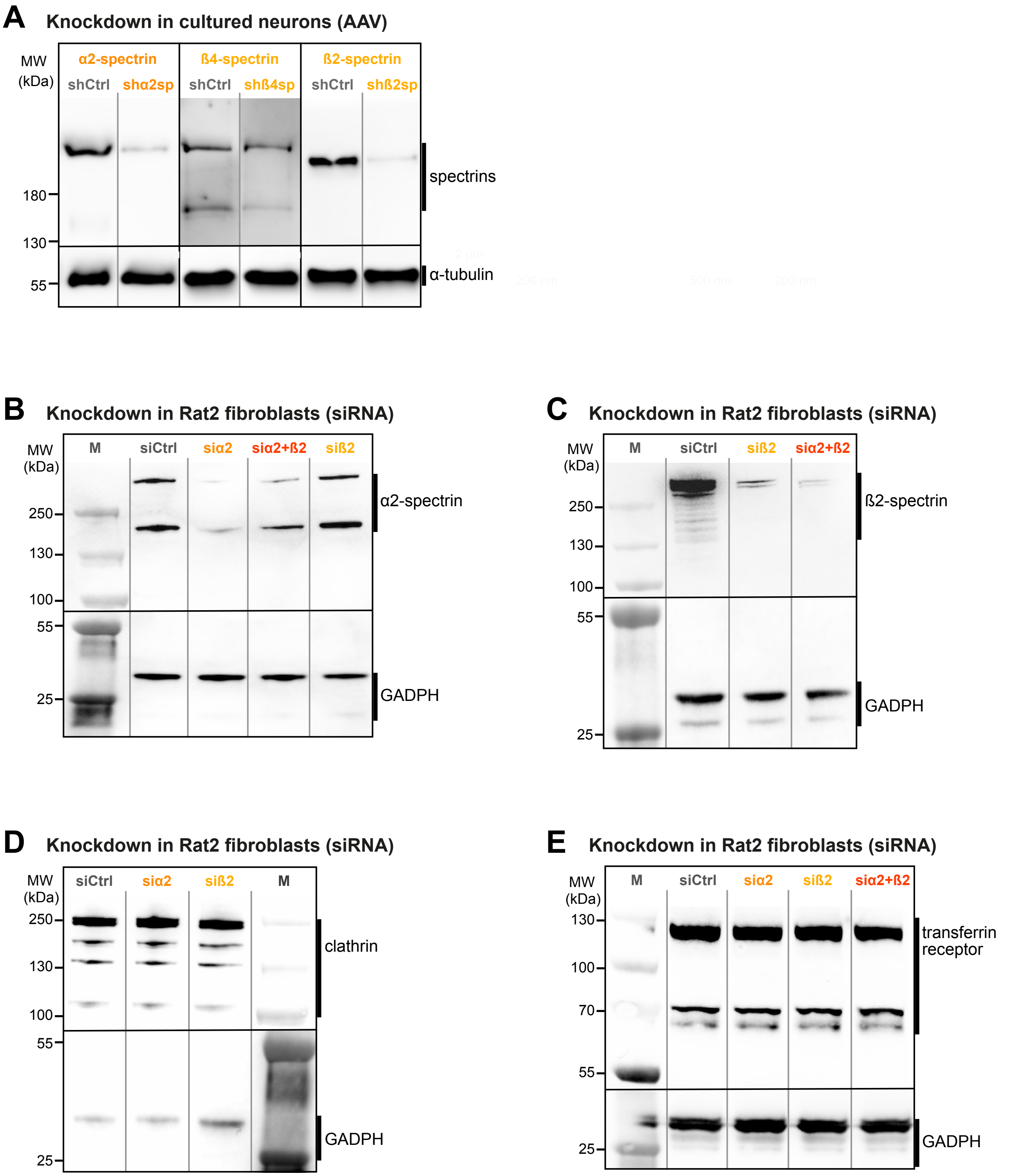

Fig. S3. siRNA and shRNA knockdown efficiency assessed by immuno blot.
(A) Immuno blots of lysates from hippocampal neurons infected with control, α2-spectrin, ß4-spectrin, or ß2-spectrin shRNA AAVs probed for α2-spectrin, ß4-spectrin, or ß2-spectrin, respectively. α-tubulin is used as a loading control (bottom). **(B)** Immuno blot of lysates from Rat2 fibroblasts transfected with control, α2-spectrin, α2+ß2-spectrin, or ß2-spectrin siRNAs probed for α2-spectrin (top), with GADPH as a loading control (bottom). **(C)** Immuno blots of lysates from Rat2 fibroblasts transfected with control, ß2-spectrin, or α2+ß2-spectrin siRNAs probed for ß2-spectrin (top), with GADPH as a loading control (bottom). **(D)** Immuno blots of lysates from Rat2 fibroblasts transfected with control, α2-spectrin, or ß2-spectrin siRNAs probed for clathrin (top), with GADPH as a loading control (bottom). Clathrin levels are unaffected by the knockdown of α2 and/or ß2-spectrin. **(E)** Immuno blots of lysates from Rat2 fibroblasts transfected with control, α2-spectrin, ß2-spectrin, or α2+ß2-spectrin siRNAs probed for transferrin receptor (TfR, top), with GADPH as a loading control (bottom). TfR levels are unaffected by the knockdown of α2 or ß2-spectrin.

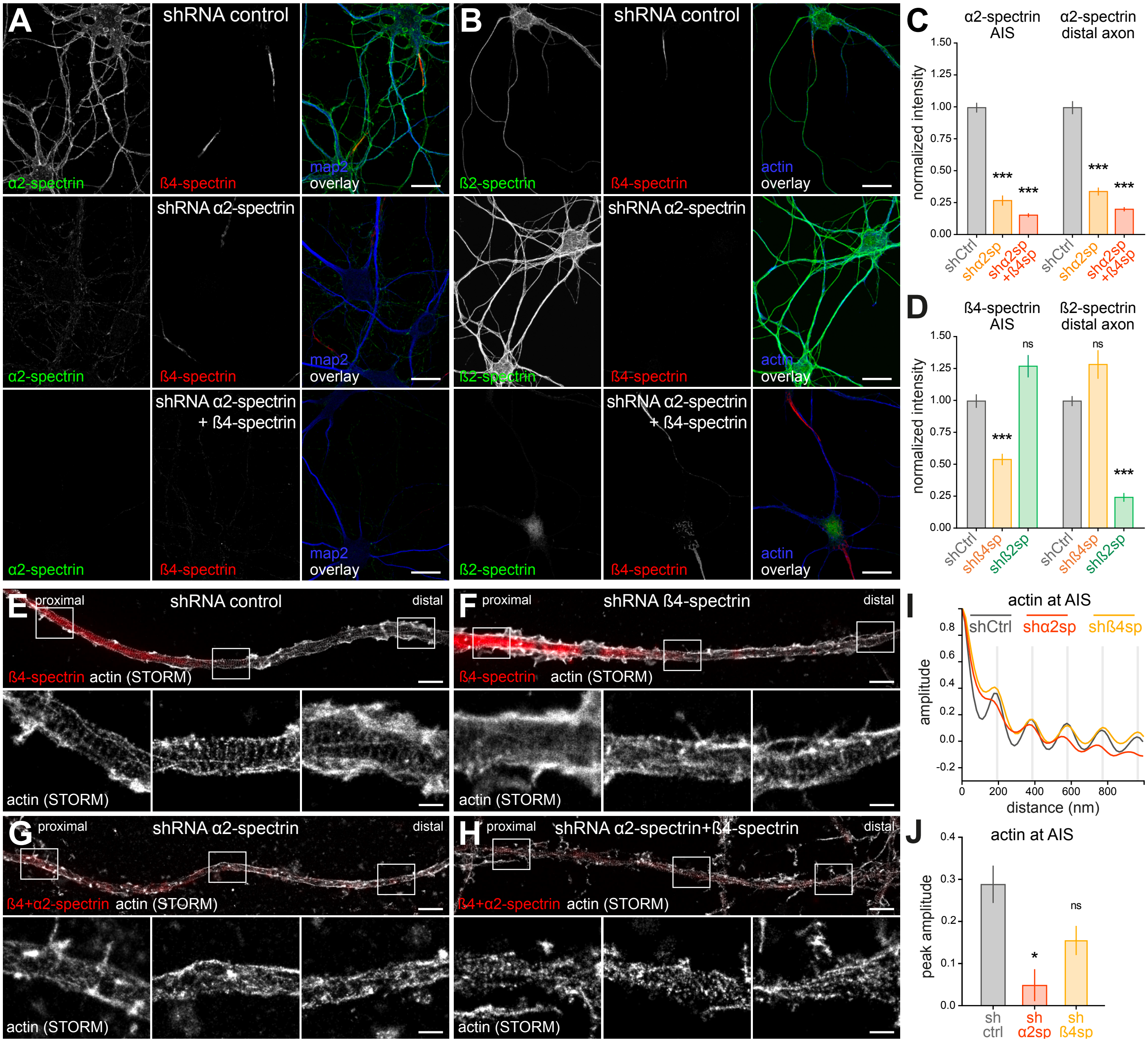

Fig. S4. Effect of spectrin knockdown in neurons assessed by immunolabeling and STORM.

(A) Epifluorescence images of cultured neurons infected with control, α2-spectrin, or α2+ß4-spectrin shRNA AAVs, fixed and stained for α2-spectrin (green), ß4-spectrin (red) and map2 (blue). **(B)** Epifluorescence images of cultured neurons infected with control, ß4-spectrin, or ß2-spectrin shRNA AAVs, fixed and stained for ß2-spectrin (green), ß4-spectrin (red) and map2 (blue). Scale bars for A and B, 20 µm. **(C)** Quantification of the normalized staining intensity for α2-spectrin at the AIS (left) and distal axon (right) in neurons infected with control, α2-spectrin, or α2+ß4-spectrin shRNA AAVs, showing the efficient knockdown of α2-spectrin in both compartments. **(D)** Quantification of the normalized staining intensity for ß4-spectrin at the AIS (left) and ß2-spectrin in the distal axon (right) in neurons infected with control, ß4-spectrin, or ß2-spectrin shRNA AAVs, showing the selective knockdown of each ß-spectrin in the AIS and distal axon. **(E)** Image of the AIS of a neuron infected with a control shRNA AAV, fixed, and stained for ß4-spectrin (red, epifluorescence image) and actin (gray, STORM image). Bottom zooms show the actin rings in the proximal, middle, and distal portions of the axon shown. Scale bar, 500 nm. **(F)** Image of the proximal axon of a neuron infected with a ß4-spectrin shRNA AAV, fixed, and stained for ß4-spectrin (red, epifluorescence image) and actin (gray, STORM image). Bottom zooms show the selective perturbation of the actin rings in the proximal portion of the axon shown. Scale bar, 500 nm. (**G**) Image of the proximal axon of a neuron infected with a α2-spectrin shRNA AAV, fixed, and stained for α2+ß4-spectrin (red, epifluorescence image) and actin (gray, STORM image). Bottom zooms show the perturbation of the actin rings in the proximal, middle, and distal portions of the axon shown. Scale bar, 500 nm. **(H)** Image of the proximal axon of a neuron infected with an α2+ß4-spectrin shRNA AAV, fixed, and stained for α2+ß4-spectrin (red, epifluorescence image) and actin (gray, STORM image). Bottom zooms show the perturbation of the actin rings in the proximal, middle, and distal portions of the axon shown. Scale bar, 500 nm. **(I)** Autocorrelation curves from intensity profiles traced along the AIS of neurons infected with control, α2-spectrin, or ß4-spectrin shRNA AAVs, fixed, stained for actin, and imaged by STORM (see E-G). Oscillations demonstrating the 190-nm periodicity (actin rings) are attenuated in α2-spectrin and ß4-spectrin knocked-down neurons. **(J)** Quantification of the first peak amplitude for the autocorrelation curves shown in I, showing lower values in α2-spectrin and ß4-spectrin knocked-down neurons.

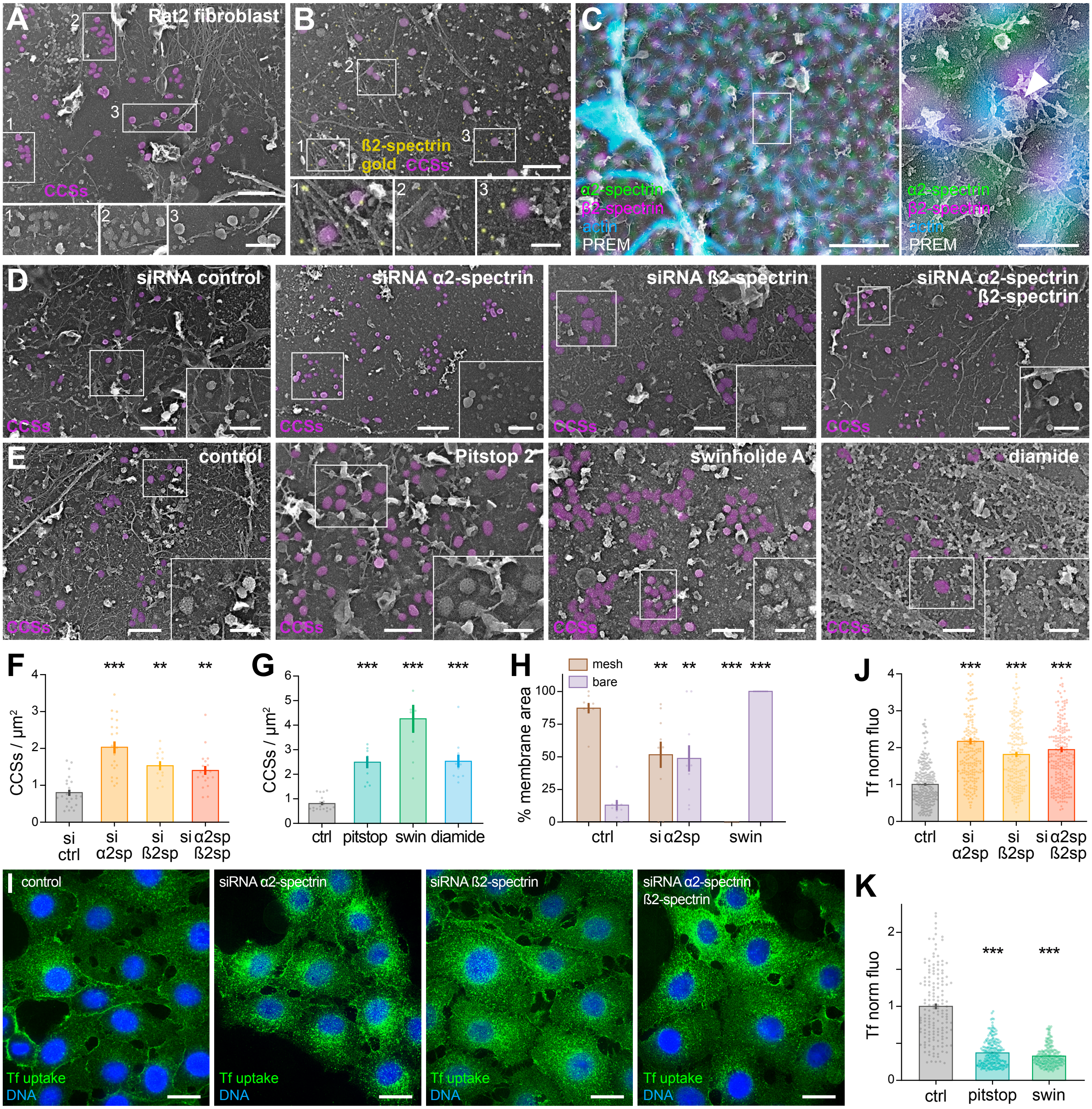

*Fig. S5. **The sparse submembrane actin-spectrin mesh restricts clathrin-coated structure formation in non-neuronal cells.*** *(See Figure on next page)* **(A)** PREM view of an unroofed Rat2 fibroblast showing the presence of clathrin-coated structures (CCSs, magenta). Bottom images are zooms of the highlighted areas in the top image. Scale bars, 2 µm (top image), 200 nm (bottom images). **(B)** PREM view of an unroofed Rat2 fibroblast immunogold-labeled for ß2-spectrin (yellow), with CCSs colored in magenta. Bottom images are zooms of the highlighted areas in the top image. Spectrins are present along the membrane, sometimes appearing as rods. Scale bars, 2 µm (top image), 200 nm (zooms). **(C)** Correlative super-resolution spinning disk microscopy-PREM of an unroofed fibroblast labeled α2-spectrin (green), ß2-spectrin (magenta), and actin (blue). Right images show a zoom of the area highlighted on the overlayed left image, with the spectrins being found along the areas rich in actin filaments, encasing a CCP (arrowhead). Scale bars, 1 µm (main image), 200 nm (zoom). **(D)** PREM views of unroofed Rat2 fibroblasts after transduction with siRNA control, against α2-spectrin, ß2-spectrin, or against α2-spectrin and ß2-spectrin, with CCSs colored in magenta on the main image. Zoom corresponds to the area highlighted on the main image. Scale bars, 5 µm (main images for siRNA against α2-spectrin and α2+ß2-spectrin), 2 µm (main image for siRNA against ß2-spectrin), 200 nm (zooms). *(See next page)*

(Continued from previous page) **(E)** PREM views of unroofed Rat2 fibroblasts after treatment with vehicle (DMS0 0.1%), swinholide A (100 nM, 3h), pitstop2 (30 µM, 15 min), or diamide (5 mM, 15 min), with CCSs colored in magenta on the main image. Zooms corresponds to the area highlighted on the main image. Scale bars, 1 µm (main images), 200 nm (zooms). **(F)** Effect of spectrins knockdown on the density of CCSs as quantified from PREM views of unroofed Rat2 fibroblasts. **(G)** Effect of drugs on the density of CCSs as quantified from PREM views of unroofed Rat2 fibroblasts. **(H)** Quantification of the submembrane organization (mesh, brown; bare plasma membrane, purple) from PREM views of fibroblasts in the control, siRNA against α2-spectrin, or swinholide A-treated conditions. **(I)** Super-resolution spinning disk microscopy images of transferrin-Alexa Fluor 488 uptake (Tf uptake, 20 µg/µL for 10 min, green) in Rat2 fibroblasts transfected with control siRNAs or against α2-spectrin, ß2-spectrin, or α2- and ß2-spectrin (from left to right), fixed and labeled with DAPI (blue). Scale bars, 10 µm. **(J)** Effect of spectrins knockdown on the intensity of Tf uptake in Rat2 fibroblasts, as quantified from spinning-disk confocal images. **(K)** Effect of drugs on the intensity of Tf uptake in Rat2 fibroblasts, as quantified from spinning-disk confocal images.

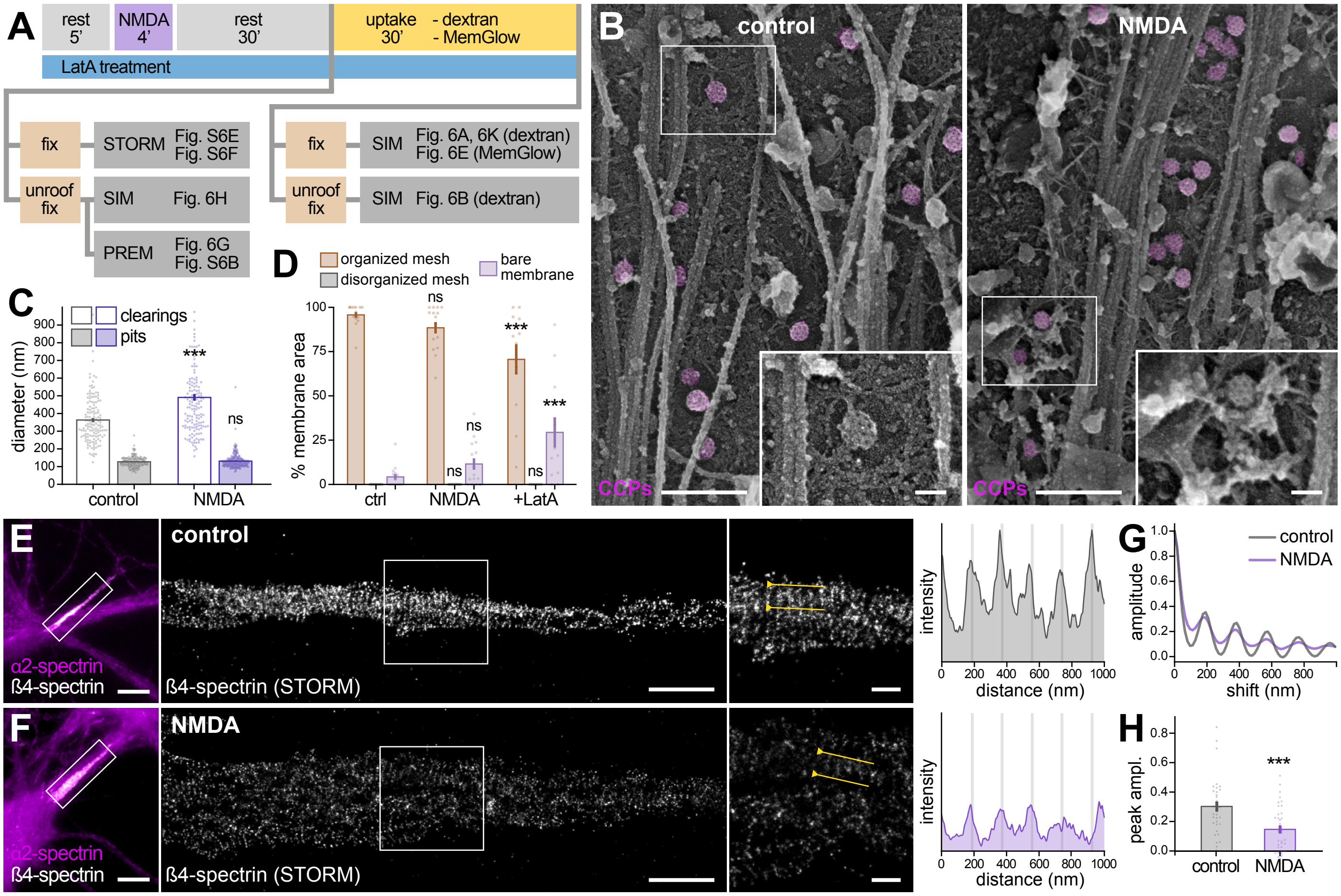

Figure S6. Effect of NMDA treatment on the actin-spectrin mesh and CCPs at the AIS.

(A) Diagram of the NMDA treatment and uptake experiments. Neurons are briefly treated with NMDA (4 min, purple) before a 30 min rest period. For morphological experiments, then are then left intact or unroofed before being fixed (bottom left). For uptake experiments, a 30 min feeding period is added allowing for fluorescent dextran or MemGlow uptake. Neurons are then left intact or unroofed before fixation (bottom right). **(B)** PREM views of the proximal axon of unroofed neurons after treatment with vehicle or NMDA, with CCPs colored in magenta. Zooms corresponds to the area highlighted on the main image. Scale bars, 500 nm (main images), 100 nm (zooms). **(C)** Quantification of the diameter for spectrin mesh clearings and for CCPs from PREM views in the control and NMDA-treated conditions. **(D)** Quantification of the submembrane organization (organized mesh, brown; disorganized mesh, gray; bare plasma membrane, purple) from PREM views of neurons in the control, NMDA-treated, NMDA+LatA-treated conditions. **(E)** Left, widefield image of a control neuron fixed and stained for α2-spectrin (magenta) and ß4-spectrin (gray). Center, STORM image of ß4-spectrin corresponding to the AIS area shown on the widefield image. Right, zoom showing the periodic organization of ß4s-spectrin with an intensity profile along the line highlighted in yellow on the zoomed image (gray bars are 185 nm apart). **(F)** Left, widefield image of a NMDA-treated neuron fixed and stained for α2-spectrin (magenta) and ß4-spectrin (gray). Center, STORM image of ß4-spectrin corresponding to the AIS area shown on the widefield image. Right, zoom showing the periodic organization of ß4s-spectrin with an intensity profile along the line highlighted in yellow on the zoomed image (gray bars are 185 nm apart). Scale bars for E and F: 10 µm (widefield image), 2 µm (STORM image), 0.5 µm (zoomed image). **(G)** Autocorrelation curves from intensity profiles traced along the AIS on STORM images of control or NMDA-treated neurons stained for ß4-spectrin. **(H)** Quantification of the first peak amplitude for the autocorrelation curves shown in G.

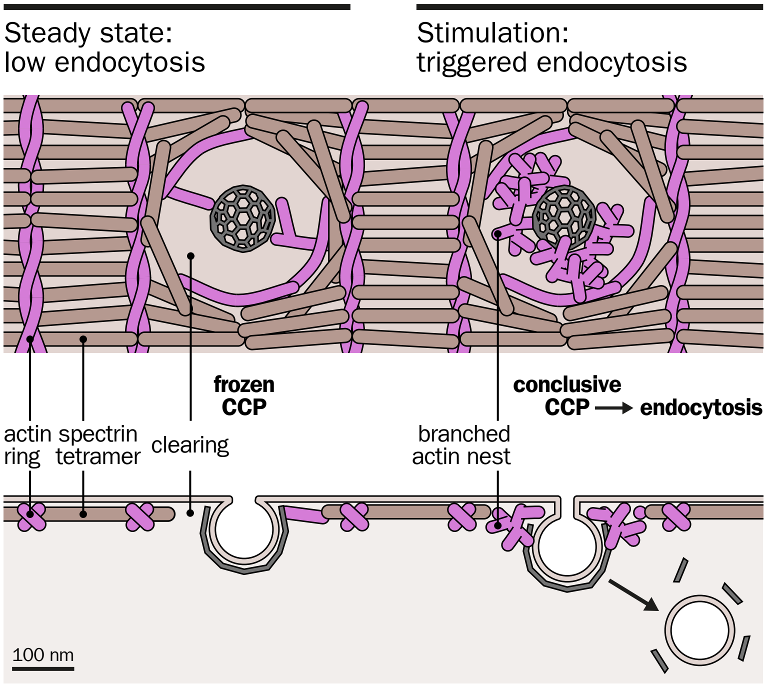

Figure S7. Endocytosis of CCPs stabilized in clearings of the AIS actin-spectrin scaffold is regulated via actin polymerization.
At steady state (left), CCPs (dark gray) are stabilized within circular clearings of the periodic actin (purple)-spectrin (brown) scaffold that lines the proximal axon plasma membrane (light brown), resulting in a low endocytosis rate. Endocytosis can be triggered in conditions such as NMDA stimulation (chemical LTD) via actin polymerization inside the clearing around the CCP, driving its scission into an intracellular vesicle (right).

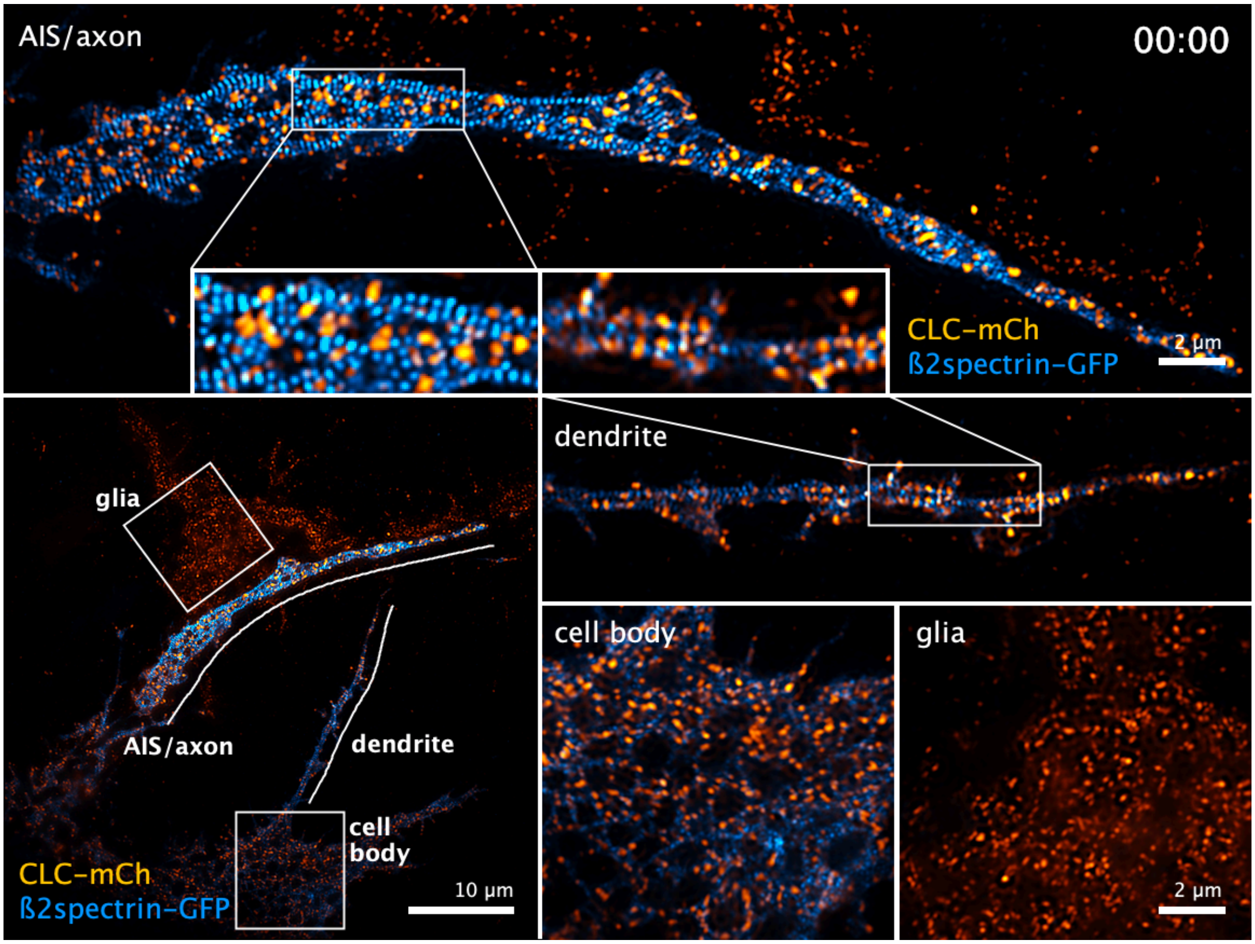

Movie S1. Dynamics of neuronal CCPs and the axonal periodic scaffold by live-cell TIRF-SIM.
Hippocampal neuron in culture transfected at 10 div with clathrin light chain-mCherry (CLC-mCh, orange) and EGFP-ß2-spectrin (ß2spectrin-GFP, blue) and imaged at 13 div by 2-color TIRF-SIM (one frame every 20s for 20 min, 61 frames total). Reconstructed TIRF-SIM images were denoised using a supervised deep-learning model trained on pairs of low and high SNR images of fixed cells expressing the same constructs (Enhance.ai). Bottom left, full-field view of the transfected neuron with highlighted areas corresponding to the AIS/proximal axon (top), dendrite (middle right), cell body (bottom center), and a neighboring glia only transfected with CLC-mCh (bottom left). Further zooms detail the dynamic of CCPs within the AIS and along the dendrite. CCPs are more stable at the AIS, being present throughout the 20-minute movie, whereas they appear more dynamic in the dendrites and cell body, and very dynamic in the glial cell.

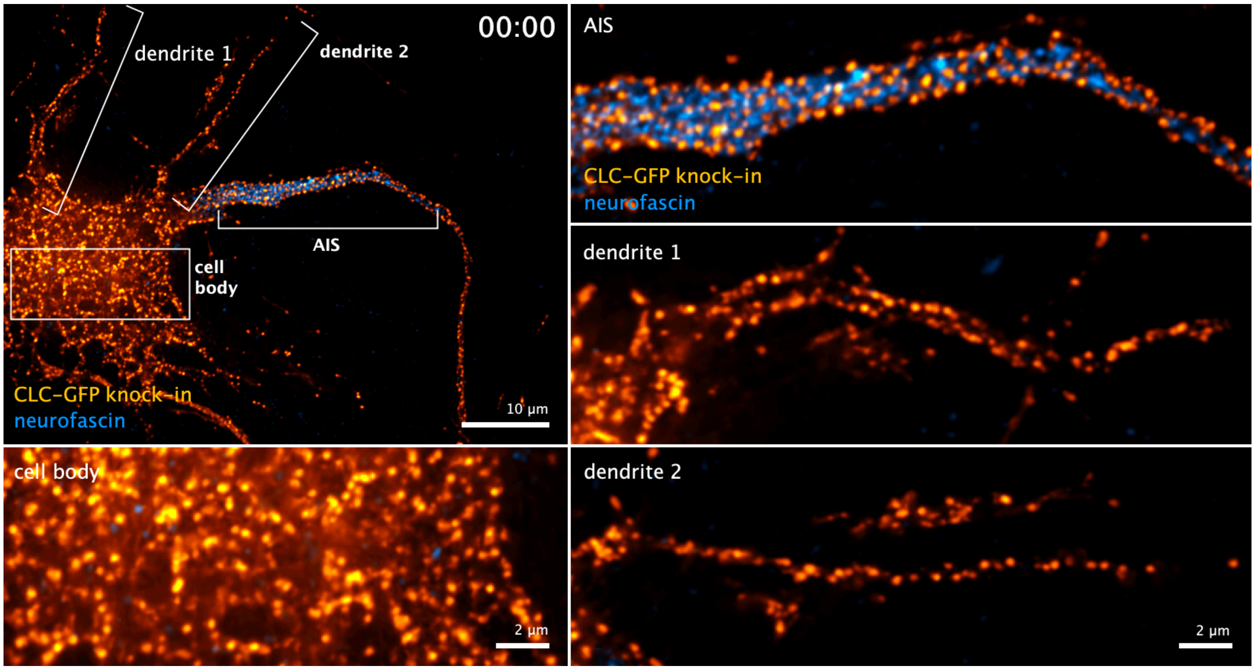

Movie S2. Dynamics of neuronal CCPs using super-resolved imaging of endogenously-tagged clathrin.
Hippocampal neuron in culture infected with AAVs targeting the endogenous tagging of clathrin light chain with EGFP at its C-terminus (CLC-GFP knock-in, orange), labeled for the AIS using an anti-neurofascin antibody targeting an extracellular epitope (blue), and imaged at 14 div using SoRa super-resolved spinning disk microscopy (one frame every 5s for 10 m, 121 images total). Raw images were denoised using a built-in deep-learning module trained on a dataset of confocal images (Denoise.ai). Top left, full-field view of the transfected neuron with highlighted areas corresponding to the AIS/proximal axon (top right), two dendrites (middle right and bottom right), and the cell body (bottom left). CCPs are more stable at the AIS compared to the dendrites and cell body.

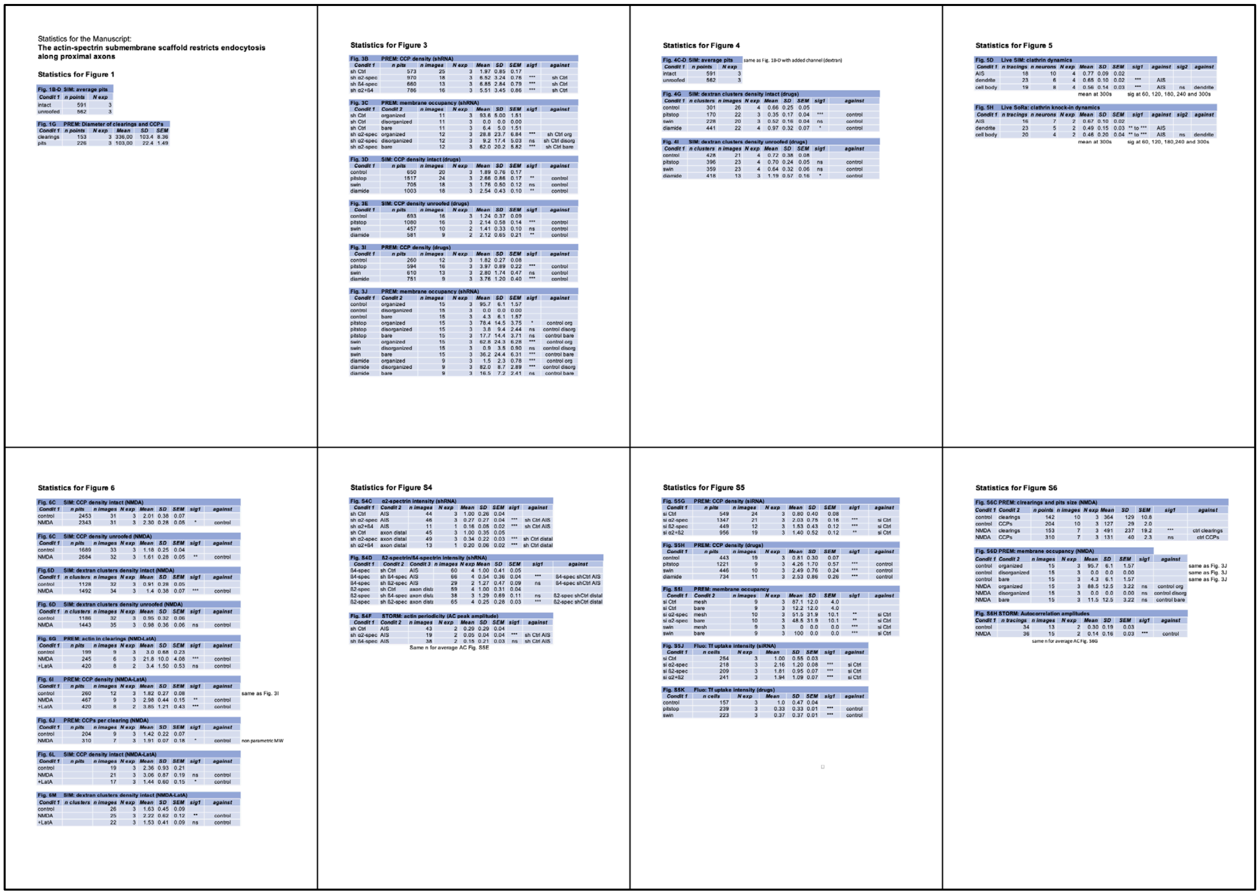

Statistics for the Manuscript:
The actin-spectrin submembrane scaffold restricts endocytosis along proximal axons

Statistics for Figure 1

Fig. 1B-D SIM: average pits

Condit 1	n points	N exp
intact	591	3
unroofed	562	3

Fig. 1G PREM: Diameter of clearings and CCPs

Condit 1	n points	N exp	Mean	SD	SEM
clearings	153	3	336,00	103.4	8.36
pits	226	3	103,00	22.4	1.49

Statistics for Figure 3

Fig. 3B PREM: CCP density (shRNA)

Condit 1	n pits	n images	N exp	Mean	SD	SEM	sig1	against
sh Ctrl	573	25	3	1.97	0.85	0.17		
sh α2-spec	970	18	3	6.52	3.24	0.76	***	sh Ctrl
sh ß4-spec	660	13	3	6.85	2.84	0.79	***	sh Ctrl
sh α2+ß4	786	16	3	5.51	3.45	0.86	***	sh Ctrl

Fig. 3C PREM: membrane occupancy (shRNA)

Condit 1	Condit 2	n images	N exp	Mean	SD	SEM	sig1	against
sh Ctrl	organized	11	3	93.6	5.00	1.51		
sh Ctrl	disorganized	11	3	0.0	0.0	0.00		
sh Ctrl	bare	11	3	6.4	5.0	1.51		
sh α2-spec	organized	12	3	28.8	23.7	6.84	***	sh Ctrl org
sh α2-spec	disorganized	12	3	9.2	17.4	5.03	ns	sh Ctrl disorg
sh α2-spec	bare	12	3	62.0	20.2	5.82	***	sh Ctrl bare

Fig. 3D SIM: CCP density intact (drugs)

Condit 1	n pits	n images	N exp	Mean	SD	SEM	sig1	against
control	650	20	3	1.89	0.76	0.17		
pitstop	1517	24	3	2.66	0.86	0.17	**	control
swin	705	18	3	1.76	0.50	0.12	ns	control
diamide	1003	18	3	2.54	0.43	0.10	**	control

Fig. 3E SIM: CCP density unroofed (drugs)

Condit 1	n pits	n images	N exp	Mean	SD	SEM	sig1	against
control	693	16	3	1.24	0.37	0.09		
pitstop	1080	16	3	2.14	0.58	0.14	***	control
swin	457	10	2	1.41	0.33	0.10	ns	control
diamide	581	9	2	2.12	0.65	0.21	**	control

Fig. 3I PREM: CCP density (drugs)

Condit 1	n pits	n images	N exp	Mean	SD	SEM	sig1	against
control	260	12	3	1.82	0.27	0.08		
pitstop	594	16	3	3.97	0.89	0.22	***	control
swin	610	13	3	2.80	1.74	0.47	ns	control
diamide	751	9	3	3.76	1.20	0.40	***	control

Fig. 3J PREM: membrane occupancy (shRNA)

Condit 1	Condit 2	n images	N exp	Mean	SD	SEM	sig1	against
control	organized	15	3	95.7	6.1	1.57		
control	disorganized	15	3	0.0	0.0	0.00		
control	bare	15	3	4.3	6.1	1.57		
pitstop	organized	15	3	78.4	14.5	3.75	*	control org
pitstop	disorganized	15	3	3.8	9.4	2.44	ns	control disorg
pitstop	bare	15	3	17.7	14.4	3.71	ns	control bare
swin	organized	15	3	62.8	24.3	6.28	***	control org
swin	disorganized	15	3	0.9	3.5	0.90	ns	control disorg
swin	bare	15	3	36.2	24.4	6.31	***	control bare
diamide	organized	9	3	1.5	2.3	0.78	***	control org
diamide	disorganized	9	3	82.0	8.7	2.89	***	control disorg
diamide	bare	9	3	16.5	7.2	2.41	ns	control bare

Statistics for Figure 4

Fig. 4C-D SIM: average pits

same as Fig. 1B-D with added channel (dextran)

Condit 1	n points	N exp
intact	591	3
unroofed	562	3

Fig. 4G SIM: dextran clusters density intact (drugs)

Condit 1	n clusters	n images	N exp	Mean	SD	SEM	sig1	against
control	301	26	4	0.66	0.25	0.05		
pitstop	170	22	3	0.35	0.17	0.04	***	control
swin	228	20	3	0.52	0.16	0.04	ns	control
diamide	441	22	4	0.97	0.32	0.07	*	control

Fig. 4I SIM: dextran clusters density unroofed (drugs)

Condit 1	n clusters	n images	N exp	Mean	SD	SEM	sig1	against
control	428	21	4	0.72	0.38	0.08		
pitstop	396	23	4	0.70	0.24	0.05	ns	control
swin	359	23	4	0.64	0.32	0.06	ns	control
diamide	418	13	3	1.19	0.57	0.16	*	control

Statistics for Figure 5

Fig. 5D Live SIM: clathrin dynamics

Condit 1	n tracings	n neurons	N exp	Mean	SD	SEM	sig1	against	sig2	against
AIS	18	10	4	0.77	0.09	0.02				
dendrite	23	6	4	0.65	0.10	0.02	***	AIS		
cell body	19	8	4	0.56	0.14	0.03	***	AIS	ns	dendrite

mean at 300s sig at 60, 120, 180, 240 and 300s

Fig. 5H Live SoRa: clathrin knock-in dynamics

Condit 1	n tracings	n neurons	N exp	Mean	SD	SEM	sig1	against	sig2	against
AIS	16	7	2	0.67	0.10	0.02				
dendrite	23	5	2	0.49	0.15	0.03	** to ***	AIS		
cell body	20	4	2	0.46	0.20	0.04	** to ***	AIS	ns	dendrite

mean at 300s sig at 60, 120, 180,240 and 300s

Statistics for Figure 6

Fig. 6C SIM: CCP density intact (NMDA)

Condit 1	n pits	n images	N exp	Mean	SD	SEM	sig1	against
control	2453	31	3	2.01	0.38	0.07		
NMDA	2343	31	3	2.30	0.28	0.05	*	control

Fig. 6C SIM: CCP density unroofed (NMDA)

Condit 1	n pits	n images	N exp	Mean	SD	SEM	sig1	against
control	1689	33	3	1.18	0.25	0.04		
NMDA	2684	32	3	1.61	0.28	0.05	**	control

Fig.6D SIM: dextran clusters density intact (NMDA)

Condit 1	n clusters	n images	N exp	Mean	SD	SEM	sig1	against
control	1128	32	3	0.91	0.28	0.05		
NMDA	1492	34	3	1.4	0.38	0.07	***	control

Fig. 6D SIM: dextran clusters density unroofed (NMDA)

Condit 1	n clusters	n images	N exp	Mean	SD	SEM	sig1	against
control	1186	32	3	0.95	0.32	0.06		
NMDA	1443	35	3	0.98	0.36	0.06	ns	control

Fig. 6G PREM: actin in clearings (NMD-LatA)

Condit 1	n pits	n images	N exp	Mean	SD	SEM	sig1	against
control	199	9	3	3.0	0.68	0.23		
NMDA	245	6	3	21.8	10.0	4.08	***	control
+LatA	420	8	2	3.4	1.50	0.53	ns	control

Fig. 6I PREM: CCP density (NMDA-LatA)

Condit 1	n pits	n images	N exp	Mean	SD	SEM	sig1	against	
control	260	12	3	1.82	0.27	0.08			same as Fig. 3I
NMDA	467	9	3	2.98	0.44	0.15	**	control	
+LatA	420	8	2	3.85	1.21	0.43	***	control	

Fig. 6J PREM: CCPs per clearing (NMDA)

Condit 1	n pits	n images	N exp	Mean	SD	SEM	sig1	against	
control	204	9	3	1.42	0.22	0.07			
NMDA	310	7	3	1.91	0.07	0.18	*	control	non parametric MW

Fig. 6L SIM: CCP density intact (NMDA-LatA)

Condit 1	n pits	n images	N exp	Mean	SD	SEM	sig1	against
control		19	3	2.36	0.93	0.21		
NMDA		21	3	3.06	0.87	0.19	ns	control
+LatA		17	3	1.44	0.60	0.15	*	control

Fig. 6M SIM: dextran clusters density intact (NMDA-LatA)

Condit 1	n clusters	n images	N exp	Mean	SD	SEM	sig1	against
control		26	3	1.63	0.45	0.09		
NMDA		25	3	2.22	0.62	0.12	**	control
+LatA		22	3	1.53	0.41	0.09	ns	control

Statistics for Figure S4

Fig. S4C α2-spectrin intensity (shRNA)

Condit 1	Condit 2	n images	N exp	Mean	SD	SEM	sig1	against
sh Ctrl	AIS	44	3	1.00	0.26	0.04		
sh α2-spec	AIS	46	3	0.27	0.27	0.04	***	sh Ctrl AIS
sh α2+ß4	AIS	11	1	0.16	0.05	0.02	***	sh Ctrl AIS
sh Ctrl	axon distal	45	3	1.00	0.35	0.05		
sh α2-spec	axon distal	49	3	0.34	0.22	0.03	***	sh Ctrl distal
sh α2+ß4	axon distal	13	1	0.20	0.06	0.02	***	sh Ctrl distal

Fig. S4D ß2-spectrin/ß4-spectrin intensity (shRNA)

Condit 1	Condit 2	Condit 3	n images	N exp	Mean	SD	SEM	sig1	against
ß4-spec	sh Ctrl	AIS	60	4	1.00	0.41	0.05		
ß4-spec	sh ß4-spec	AIS	66	4	0.54	0.36	0.04	***	ß4-spec shCtrl AIS
ß4-spec	sh ß2-spec	AIS	29	2	1.27	0.47	0.09	ns	ß4-spec shCtrl AIS
ß2-spec	sh Ctrl	axon dist	59	4	1.00	0.31	0.04		
ß2-spec	sh ß4-spec	axon dist	38	3	1.29	0.69	0.11	ns	ß2-spec shCtrl distal
ß2-spec	sh ß2-spec	axon dist	65	4	0.25	0.28	0.03	***	ß2-spec shCtrl distal

Fig. S4F STORM: actin periodicity (AC peak amplitude)

Condit 1	Condit 2	n images	N exp	Mean	SD	SEM	sig1	against
sh Ctrl	AIS	43	2	0.29	0.29	0.04		
sh α2-spec	AIS	19	2	0.05	0.04	0.04	***	sh Ctrl AIS
sh ß4-spec	AIS	38	2	0.15	0.21	0.03	ns	sh Ctrl AIS

Same n for average AC Fig. S5E

Statistics for Figure S5

Fig. S5G PREM: CCP density (siRNA)

Condit 1	n pits	n images	N exp	Mean	SD	SEM	sig1	against
si Ctrl	549	24	3	0.80	0.40	0.08		
si α2-spec	1347	21	3	2.03	0.75	0.16	***	si Ctrl
si ß2-spec	449	12	3	1.53	0.43	0.12	***	si Ctrl
si α2+ß2	956	19	3	1.40	0.52	0.12	**	si Ctrl

Fig. S5H PREM: CCP density (drugs)

Condit 1	n pits	n images	N exp	Mean	SD	SEM	sig1	against
control	443	19	3	0.81	0.30	0.07		
pitstop	1221	9	3	4.26	1.70	0.57	***	control
swin	446	10	3	2.49	0.76	0.24	***	control
diamide	734	11	3	2.53	0.86	0.26	***	control

Fig. S5I PREM: membrane occupancy

Condit 1	Condit 2	n images	N exp	Mean	SD	SEM	sig1	against
si Ctrl	mesh	9	3	87.1	12.0	4.0		
si Ctrl	bare	9	3	12.2	12.0	4.0		
si α2-spec	mesh	10	3	51.5	31.9	10.1	**	si Ctrl
si α2-spec	bare	10	3	48.5	31.9	10.1	**	si Ctrl
swin	mesh	9	3	0	0.0	0.0	***	si Ctrl
swin	bare	9	3	100	0.0	0.0	***	si Ctrl

Fig. S5J Fluo: Tf uptake intensity (siRNA)

Condit 1	n cells	N exp	Mean	SD	SEM	sig1	against
si Ctrl	254	3	1.00	0.55	0.03		
si α2-spec	218	3	2.16	1.20	0.08	***	si Ctrl
si ß2-spec	209	3	1.81	0.95	0.07	***	si Ctrl
si α2+ß2	241	3	1.94	1.09	0.07	***	si Ctrl

Fig. S5K Fluo: Tf uptake intensity (drugs)

Condit 1	n cells	N exp	Mean	SD	SEM	sig1	against
control	157	3	1.0	0.47	0.04		
pitstop	239	3	0.33	0.33	0.01	***	control
swin	223	3	0.37	0.37	0.01	***	control

Statistics for Figure S6

Fig. S6C PREM: clearings and pits size (NMDA)

Condit 1	Condit 2	n points	n images	N exp	Mean	SD	SEM	sig1	against
control	clearings	142	10	3	364	129	10.8		
control	CCPs	204	10	3	127	29	2.0		
NMDA	clearings	153	7	3	491	237	19.2	***	ctrl clearings
NMDA	CCPs	310	7	3	131	40	2.3	ns	ctrl CCPs

Fig. S6D PREM: membrane occupancy (NMDA)

Condit 1	Condit 2	n images	N exp	Mean	SD	SEM	sig1	against	
control	organized	15	3	95.7	6.1	1.57			same as Fig. 3J
control	disorganized	15	3	0.0	0.0	0.00			same as Fig. 3J
control	bare	15	3	4.3	6.1	1.57			same as Fig. 3J
NMDA	organized	15	3	88.5	12.5	3.22	ns	control org	
NMDA	disorganized	15	3	0.0	0.0	0.00	ns	control disorg	
NMDA	bare	15	3	11.5	12.5	3.22	ns	control bare	

Fig. S6H STORM: Autocorrelation amplitudes

Condit 1	n tracings	n images	N exp	Mean	SD	SEM	sig1	against
control	34	13	2	0.30	0.19	0.03		
NMDA	36	15	2	0.14	0.16	0.03	***	control

same n for average AC Fig. S6G

Data S1. Statistics for the graphs and quantitative data shown in Figures.
Spreadsheet file containing the statistics (mean, SEM, number of points, number of independent experiments, significance tests) for all values shown in Figures and Supplementary Figures.